### Spatiotemporal Modeling of Mitochondrial Network Architecture

Keaton B. Holt<sup>®</sup>, <sup>1</sup> Julius Winter<sup>®</sup>, <sup>2</sup> Suliana Manley<sup>®</sup>, <sup>2</sup> and Elena F. Koslover<sup>®</sup>, <sup>1</sup> Department of Physics, University of California, San Diego, La Jolla, California 92093, USA <sup>2</sup> Institute of Physics, École Polytechnique Fédérale de Lausanne (EPFL), Lausanne, Switzerland

(Received 24 January 2024; accepted 12 September 2024; published 8 October 2024)

In many cell types, mitochondria undergo extensive fusion and fission to form dynamic, responsive network structures that contribute to a number of homeostatic, metabolic, and signaling functions. The relationship between the dynamic interactions of individual mitochondrial units and the cell-scale network architecture remains an open area of study. In this work, we use coarse-grained simulations and approximate analytic models to establish how the network morphology is governed by local mechanical and kinetic parameters. The transition between fragmented structures and extensive networks is controlled by local fusion-to-fission ratios, network density, and geometric constraints. Similar fusion rate constants are found to account for the very different structures formed by mammalian networks (poised at the percolation transition) and well-connected budding yeast networks. Over a broad parameter range, the simulated network structures can be described by effective mean-field association constants that exhibit a nonlinear dependence on the microscopic nonequilibrium fusion, fission, and transport rates. Intermediate fusion rate constants are shown to result in the highest rates of network remodeling, with mammalian mitochondrial networks situated in a regime of high turnover. This spatially resolved modeling and simulation framework helps elucidate the emergence of cellular scale network structures, and allows for the quantitative extraction of microscopic kinetic parameters from past and future experimental data.

### DOI: 10.1103/PRXLife.2.043002

### I. INTRODUCTION

Eukaryotic cells rely on mitochondria, pleomorphic organelles specialized for ATP production, to supply their metabolic needs. In addition to their role as an energetic powerhouse, mitochondria participate in a broad array of cellular functions, including Ca<sup>2+</sup> homeostasis, lipid storage and production, and programed cell death [1]. In recent decades, the physical structure of mitochondria has been found to be vitally intertwined with cellular function, state, and health [2–6]. Across a variety of cell types, mitochondria are observed to form dynamic, interconnected spatial networks which rearrange on the order of seconds [7] through fusion and fission of mitochondrial membranes, and motion of the organelles through the intracellular space [8–10]. These networks can exhibit a variety of structures, including three-dimensional partially fragmented architectures in mammalian cells [7], and cortical surface-bound extensively connected networks in yeast cells [11].

The formation of interconnected mitochondrial networks is implicated in a host of cellular functions [12]. These include protection against stress and perturbations to membrane potential [13], modulation of ATP production rate and

Published by the American Physical Society under the terms of the Creative Commons Attribution 4.0 International license. Further distribution of this work must maintain attribution to the author(s) and the published article's title, journal citation, and DOI.

efficiency [14], and regulation of calcium signaling [15]. The networked mitochondrial architecture is also thought to play an important role in quality control [3,12,16]. Mitochondrial proteins and DNA are particularly prone to oxidative damage as a result of high respiration rates, with the mutation rate of human mitochondrial DNA (mtDNA) estimated as roughly 400-fold higher than in the nucleus [17]. Fusion and fission enable mitochondria to share their contents [18], allowing for potential complementation of damaged components [19,20]. In addition, dynamic remodeling of the mitochondrial network, together with selective fusion [2], fission [21], and/or autophagy [9,22], makes it possible to segregate and recycle damaged mitochondria, improving the health of the overall population.

When quality control is dysfunctional, accumulated damage to mtDNA and mitochondrial proteins over multiple cell cycles leads to loss of mitochondrial function, a decline which is associated with ageing [23]. Decreased mitochondrial function, coupled with modification of network structure, is also associated with neurological diseases such as Alzheimer's [24], Parkinson's [25], and Huntington's disease [26]. Fragmented mitochondrial networks are frequently observed in each of these pathologies, suggesting impairment of the fusion and fission machinery [27]. Indeed, induced overexpression of fusion proteins or repression of fission proteins may rescue the normal phenotype from an initially diseased cell state [28].

Mitochondrial network structure can be altered by genetic and pharmacological interventions as well as nutrient and environmental conditions. The upregulation or overexpression of mitochondrial fusion proteins (MFN1, MFN2, OPA1 in

<sup>\*</sup>Contact author: ekoslover@ucsd.edu

mammalian cells and Fzo1, Mgm1 in yeast [3]) can lead to hyperfused, highly connected networks [6,29], and may counteract pathological fragmentation [28]. Genetic disruption of fission proteins [30] (DRP1, Dnm1 in mammalian and yeast cells, respectively [3]) also leads to mitochondrial elongation, while treatment with toxins such as oligomycin [7], FCCP [31], and paraquat [29] induces fragmentation of the network. Nutrient availability has been shown to regulate mitochondrial network volume [32] and structure. Cells grown in excess glucose undergo mitochondrial fragmentation [14], while those in a state of nutrient deprivation exhibit increased mitochondrial tubulation and connectivity [33]. Such tubulation is generally accompanied by altered intra-mitochondrial structure, with a higher density of cristae junctions on the inner membrane leading to increased ATP synthesis [4,34]. The connectivity of the mitochondrial network has thus been shown to correlate directly with its efficiency in ATP production [6].

Recent advances in imaging technology have allowed for real-time tracking and quantification of mitochondrial network structure [6,7,11,35]. However, advances in theoretical modeling are needed to consolidate the data into a quantitative framework and push foward our understanding of the physical processes and principles that govern these dynamic structures. Previous models have largely relied on aspatial [36,37], continuum [38], lattice-based [12], or two-dimensional [9,39] approaches. These computational studies complement experimental quantifications of mitochondrial architecture [6,11] to link the observed steady-state network structure with cellularscale global frequencies of fusion and fission. Several past theoretical works have also explored the ability of networks to distribute or segregate mitochondrial contents [9,12,37,39]. Nevertheless, the impact of mitochondrial mechanics, local intrinsic interaction kinetics, and transport dynamics on network structure remains opaque.

The fusion and fission of mitochondrial units is in many ways analogous to reversible clustering in molecular-scale systems. Past work on molecular aggregation has examined the structures formed by interacting monomers undergoing Brownian motion. In models of reversible aggregation, the probabilities to form and break bonds between monomers control the properties of the resulting structure [40]. Other formulations rely on a temperature-dependent short-range attraction between colliding monomers to hold the structure together [41]. Above a critical value of the bonding probability or attraction strength, called the percolation threshold, most particles will be members of a single supercluster [42,43]. The percolation threshold has been extensively studied for systems of various constituent particle shapes such as spheres [44], ellipsoids [45], and spherocylinders [46]. Other studies have examined the role of particle mobility on structure [47,48], finding that increased mobility leads to a higher degree of compactness. Notably, mitochondrial networks differ from many previously studied clustering systems in that their fusion and fission processes are energy-driven and thus out of thermal equilibrium. This energy consumption has the potential to break some of the thermodynamic constraints linking mitochondrial motility, flexibility, and the configuration-dependent fusion-fission balance, thereby altering the relationship between network morphology and microscopic dynamics.

Here we use theoretical modeling to ask how local interactions between individual pairs of mitochondria, together with the motion of the organelles through space, gives rise to emergent large-scale network structures. In particular, we elucidate the relationship between microscopic parameters such as the fusion rate constant for adjacent mitochondria, the bending stiffness of the mitochondrial tubules, and the mobility of individual mitochondria, with macroscopic metrics such as the segment length and connectivity of the resulting network. We find that network structures below or near percolation can be approximately predicted from microscopic rate constants, in both three-dimensional (3D) and surfacebound systems and demonstrate that intermediate fusion rate constants allow for the most rapid rearrangement of network structure. These results lay the groundwork for developing a fundamental mechanistic understanding of how diverse experimental perturbations to mitochondrial morphogens modulate the overall dynamics, and thereby the health and function, of the network.

#### II. MODEL DESCRIPTION

We model the mitochondrial network using a 3D, dynamic, graph-based formulation in which edges represent discrete mitochondrial units of ground-state length  $\ell_0 = 0.5 \,\mu m$  and steric radius  $r_s = 0.1 \, \mu \text{m}$ . The effect of increasing mitochondrial thickness is considered in the Supplemental Material (Fig. S5) [49]. While estimates of minimal mitochondrial size vary, the literature suggests a tubule width in the range of 200-500 nm, and a diameter of 300-500 nm for the smallest isolated spherical mitochondria [36,55–57]. As the simulated mitochodrial units are all rod shaped, we chose  $\ell_0$  such that the volume of isolated units is comparable to that of the smallest reported spherical mitochondria. Nodes represent the endpoints of each mitochondrion and serve as the locations where forces are applied and fusion-fission events can occur. The positions of the nodes evolve over time according to an overdamped Langevin equation:

$$\mu \frac{d\vec{r}}{dt} = \vec{F}^{(B)} + \vec{F}^{(\text{mech})},\tag{1}$$

$$\vec{F}^{(\text{mech})} = -\partial_{\vec{r}}(E_{\text{bend}} + E_{\text{stretch}} + E_{\text{steric}} + E_{\text{conf}}),$$
 (2)

with  $\mu$  the friction coefficient for each node,  $\vec{r}$  the vector of node positions, and  $\vec{F}^{(B)}$  and  $\vec{F}^{(mech)}$  corresponding to the Brownian and mechanical forces, respectively. The stochastic Brownian forces are uncorrelated in time:  $\langle F_{i,j}^{(B)} F_{i_2,j_2}^{(B)} \rangle = 2k_b T \delta_{i_1,i_2} \delta_{j_1,j_2}$ , where i refers to the node index, j to the spatial dimension, and  $k_b T$  is the thermal energy.

The bending energy is defined by:

$$E_{\text{bend}} = -\frac{B_1}{\ell_0} \sum_{i \in \{\text{deg } 2\}} \cos \theta_i - \frac{B_2}{\ell_0} \sum_{i \in \{\text{deg } 3\}} \sum_{j=1}^3 \cos \left(\theta_i^{(j)} - \frac{\pi}{3}\right),$$
(3)

where the first term depends on the deviation of each degree-2 node from a straight configuration and the second term depends on the deviation of each angle in a degree-3 junction from its ground-state value of 60° (see Supplemental Material Fig. S2) [49]. The mechanical

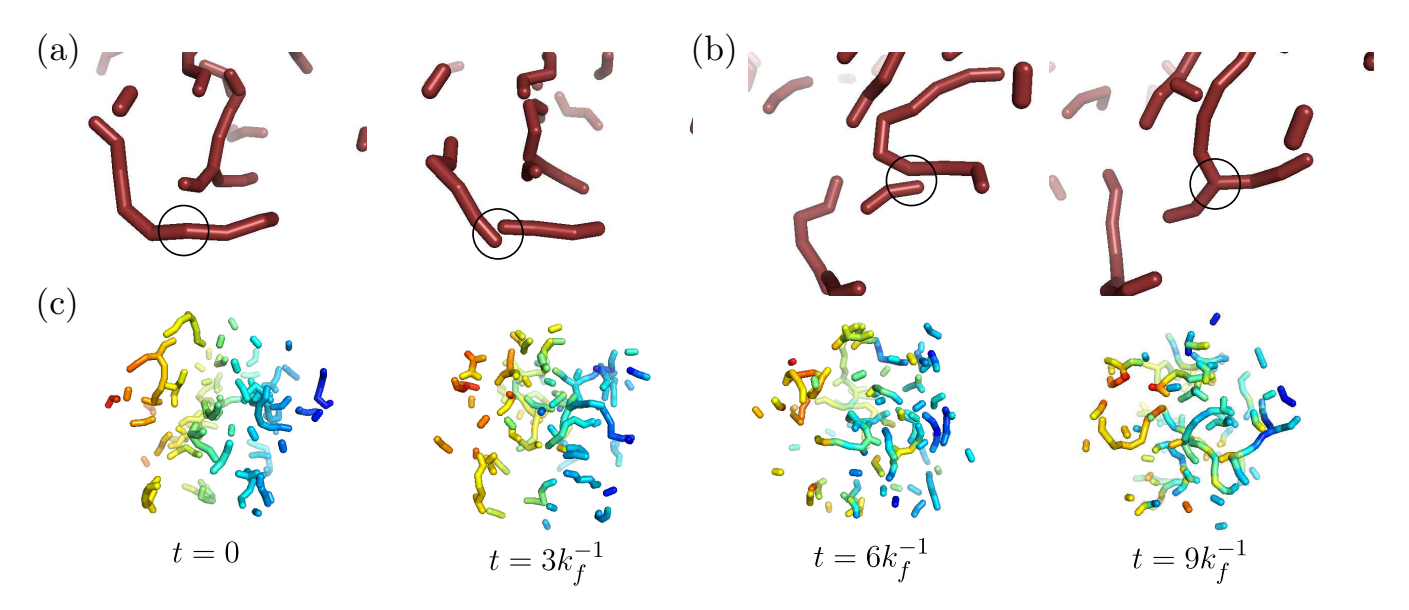


FIG. 1. Fission and fusion reshape the mitochondrial network. (a) An example of tip-tip fission at a degree-2 node. (b) An example of tip-side fusion to form a degree-3 junction. (c) Snapshots of an example mitochondrial network simulation. Edges are colored according to their initial position to visualize mixing.

energy also includes quadratic penalties for each edge length deviating from its ground state value ( $E_{\rm stretch}$ ), for two nonconnected edges approaching closer than the minimal steric distance ( $E_{\rm steric}$ ), and for any node escaping a spherical confinement ( $E_{\rm conf}$ ). This coarse-grained model subsumes the many complex details of deforming mitochondrial membranes into a handful of effective parameters, analogously to commonly used bead-rod models for biopolymers [58,59]. Details of the energetic terms, the choice of default parameters, and the time integration of Eq. (1) are given under Methods.

Topological remodeling of the network is implemented via local fusion and fission events at the nodes [Figs. 1(a) and 1(b)]. We assume that fusion may only occur between a pair of degree-1 nodes (tip-tip fusion) or between a degree-1 and a degree-2 node (tip-side fusion). This limits the network to nodes of degrees 1–3, in keeping with prior work showing that higher-degree nodes are rarely observed in mitochondrial networks [29,36]. Fusion is allowed when the nodes are separated by a distance  $\leq 2r_c$ , where  $r_c$  is the contact radius. During the time that the nodes are in contact, fusion kinetics are controlled by rate constants for tip-tip and tip-side fusion events  $(k_{u1}^{\text{eff}}, k_{u2}^{\text{eff}}, \text{ respectively})$  with dimensions of inverse time. We note these microscopic rate constants cannot be mapped directly onto the fusion frequency reported in the literature [60], which corresponds to the total number of observed fusion events per time per mitochondrial quantity. The rate constants used here are fundamental kinetic parameters which are independent of the number, volume density, and transport rate of mitochondria.

The microscopic fusion rate constants are taken to be dependent on the orientation of the fusing edges, precluding fusion events that lead to very high bending energies. The implicit assumption is that fusion machinery on the mitochondrial surface can only perform its function if the mitochondrial segments are favorably aligned. By default, we make the

fusion rate constants for tip-tip and tip-side fusion ( $k_{u1}^{\text{eff}}$ ,  $k_{u2}^{\text{eff}}$ , respectively) proportional to a Boltzmann factor incorporating the relevant bending energies:

$$k_{u1}^{\text{eff}}(\theta) = k_{u1}e^{-\alpha_1(1-\cos\theta)},$$

$$k_{u2}^{\text{eff}}(\theta^{(2)}, \theta^{(3)}) = k_{u2}e^{-\alpha_2[2-\cos(\theta^{(2)}-\pi/3)-\cos(\theta^{(3)}-\pi/3)]},$$
(4b)

where  $\theta$  is the angle formed by the edges meeting at the new degree-2 node and  $\theta^{(2)}$ ,  $\theta^{(3)}$  are the angles formed by the incoming third edge relative to the existing edges making up the former degree-2 junction. As with the mechanical bending at the three way junction, angles of  $\pi/3$  are assumed to be preferred for fusion. However, for degree-3 junction formation, only the two angles involving the newly added segment are used to define the fusion rate constant. The parameters  $k_{ui}$  set the fusion rate constant when all edges are perfectly aligned, while  $\alpha_i$  sets the sensitivity of the fusion machinery to deviations from the preferred junction angles.

The angular dependence of fusion rate constants has not been empirically established. The form selected here satisfies the general principle of permitting fusion only when it will not lead to large energy penalties at the newly formed junctions. The default angle-sensitivities are set to  $\alpha_i = B_i/(\ell_0 k_b T)$ . For the degree-2 case this is the expected behavior for a system in thermal equilibrium, where fusion and fission obey detailed balance. For the degree-3 case, detailed balance is broken because the fusion rate constant excludes the change in energy associated with the pre-existing junction angle.

Fission occurs at nonterminal network nodes, with a rate of  $k_f$  for degree-2 nodes and  $\frac{3}{2}k_f$  for degree-3 junctions. In keeping with prior models [36], these rates assume that the fission machinery docks on the edges surrounding the junction, so that fission is proportionally more likely to occur at a junction with three adjacent edges. Following fission of a degree-2 node, the tips of the resulting segments (defined as one steric

radius beyond the new degree-1 node positions) meet at the former node location. During fission at a degree-3 junction, one edge is selected at random to break from the others. The newly formed tip of this edge is placed at the former junction while the remaining degree-2 node is moved away in the opposite direction from the original junction by a distance  $r_s$  (the steric radius). This approach ensures that a very rapid fission and refusion event would result in no net change in the mechanical energetics at the junction. Details of the fusion and fission processes are illustrated in Supplemental Material [49].

The dynamic model is evolved forward in time using Brownian dynamics simulations, with the appropriate probabilities of fusion and fission at each time step based on the remodeling rates defined above. The simulations are carried out in dimensionless units, with the length scale set by  $2\ell_0 = 1$ , the timescale by  $1/k_f = 1$  (where  $k_f$  is a fission rate constant, discussed below), and the force scale by  $\mu = 1$ .

To convert to real units, we estimate  $k_f \approx 0.5 \text{ min}^{-1}$ . As discussed under Results, this gives an overall rate of "complete fission" (not followed by refusion to the same node) on the order of 0.1 per minute per mitochondrion, consistent with prior experimental and modeling studies [2,9,37,61–63]. The default effective temperature is set to  $k_bT=1$  in dimensionless units, yielding a diffusivity for an isolated mitochondrial edge unit of  $D_1=0.25 \ \mu\text{m}^2/\text{min}$ , consistent with measurements of stochastic mitochondrial motion within mammalian cells [7,64,65].

The resulting network configurations rearrange over timescales governed by the fusion and fission rate constants as well as the effectively diffusive movement of the mitochondrial units. Substantial rearrangements of network topology occur over a time period of a few minutes [Fig. 1(c), Supplemental Video 1].

### III. RESULTS

### A. Network architecture emerges from the balance of fusion and fission

As with molecular clustering systems that undergo reversible aggregation [40,66], the steady-state structure of the simulated mitochondrial network depends on the ratio of local fusion and fission rate parameters  $k_{ui}/k_f$  (Fig. 2). For a fixed fission rate, and low fusion, the mitochondria are largely fragmented into small disjoint segments. At higher fusion, networks become well connected, containing numerous degree-2 nodes and degree-3 junctions. When the fusion rate constants are similar ( $k_{u2} = k_{u1}$ ), degree-3 junctions dominate within well-connected networks [Fig. 2(a), left]. By contrast, when the tip-side fusion rate is reduced ( $k_{u2} = 0.1k_{u1}$ ), there is a broad intermediate regime with long linear chains containing many degree-2 nodes and only a small number of degree-3 junctions [Fig. 2(a), right].

In keeping with prior measurements of mitochondrial networks [6,11,29,36], we quantify the network architecture using two experimentally accessible metrics. The largest cluster size fraction  $\langle L_G/L \rangle$  is defined as the mitochondrial length in the largest connected component of the network, normalized by the total mitochondrial length. This metric

quantifies the overall network connectivity, with a value of 1 indicating a fully connected structure and low values corresponding to fragmented populations. As the tip-side fusion rate constant  $k_{u2}$  is dialed up, the system undergoes a percolation transition with network fragments coalescing into a single supercluster. This is indicated by the sharp jump in  $\langle L_G/L \rangle$  [Fig. 2(b)]. Notably, the onset of percolation is shifted to higher values of  $k_{u2}$  when the tip-tip fusion rate constant is reduced, due to the ensuing scarcity of degree-2 nodes necessary for forming junctions. Near the percolation transition, small changes in the fusion rate constant can greatly alter the network architecture. Previous studies have indicated that mammalian mitochondrial networks tend to balance near this percolation threshold [29,36,67], allowing for profound alterations in network morphology in response to small environmental changes.

A separate structural metric is the mean segment length  $\langle L_{\rm seg} \rangle = \ell_0 N_{\rm edge} / N_{\rm seg}$ , where a segment is defined as a linear chain of mitochondrial units, terminating at either a degree-1 node or a degree-3 junction. The number of segments can be computed as  $N_{\rm seg} = N_{\rm edge} - N_{\rm degree-2\ nodes} + N_{\rm free\ loops}$ , where a free loop is a connected component containing only degree-2 nodes. A large value of  $\langle L_{\rm seg} \rangle$  indicates the presence of numerous extended linear mitochondria with few branches. Notably, a maximally connected network (containing entirely branching nodes) and a completely fragmented network (only degree-1 nodes) have the same mean segment length (unit length  $\ell_0 = 0.5\ \mu m$ ). High values of  $\langle L_{\rm seg} \rangle$  require tip-tip fusions to dominate, with  $k_{u1} \gg k_{u2}$  [Fig. 2(c)].

By varying both microscopic fusion rate constants (relative to a fixed fission rate constant  $k_f$ ), a broad region of the two structural features  $(\langle L_G/L \rangle)$  and  $\langle L_{\rm seg} \rangle$  can be accessed [Fig. 2(d)]. For a given largest cluster size, the mean segment length can be tuned by altering the ratio of tip-side versus tip-tip fusion constants  $(k_{u2}/k_{u1})$ . High values of this ratio (yellow curve) give networks with very short segment lengths across the entire spectrum of connectivity. Low values of the ratio (purple curve) allow for long segment lengths throughout an intermediate regime where networks are neither fully fragmented nor fully percolated.

We identify the experimentally relevant fusion parameters by comparing with published mitochondrial network structures from a set of 93 images of a human induced pluripotent stem cell (hiPSC, provided in Ref. [7]) and from 37 images of COS-7 cells grown on patterns (obtained as described under Methods). These networks [Fig. 2(e)] have mean segment lengths of  $\langle L_{\rm seg} \rangle \approx 1.19, 1.24~\mu {\rm m}$  and largest cluster fraction  $\langle L_G/L \rangle \approx 0.18, 0.08$ , respectively. Both mammalian cell types yield consistent estimates of the relative fusion parameter ratio:  $k_{u2}/k_{u1} \approx 0.3 \pm 0.06$ , and  $0.2 \pm 0.1$ , respectively. For this ratio of tip-side to tip-tip fusion rate constants, percolation of the network occurs at  $k_{u2}/k_f \approx 600$ , where  $k_f \approx 0.5~{\rm min}^{-1}$  sets the rate units in the simulations.

The tip-tip versus tip-side microscopic fusion rate constants for spatially proximal and orientationally well-aligned segments are thus expected to be quite similar in magnitude. This estimate is in stark contrast to the overall global association constants predicted in prior work, which indicated a global tip-side fusion rate that was lower

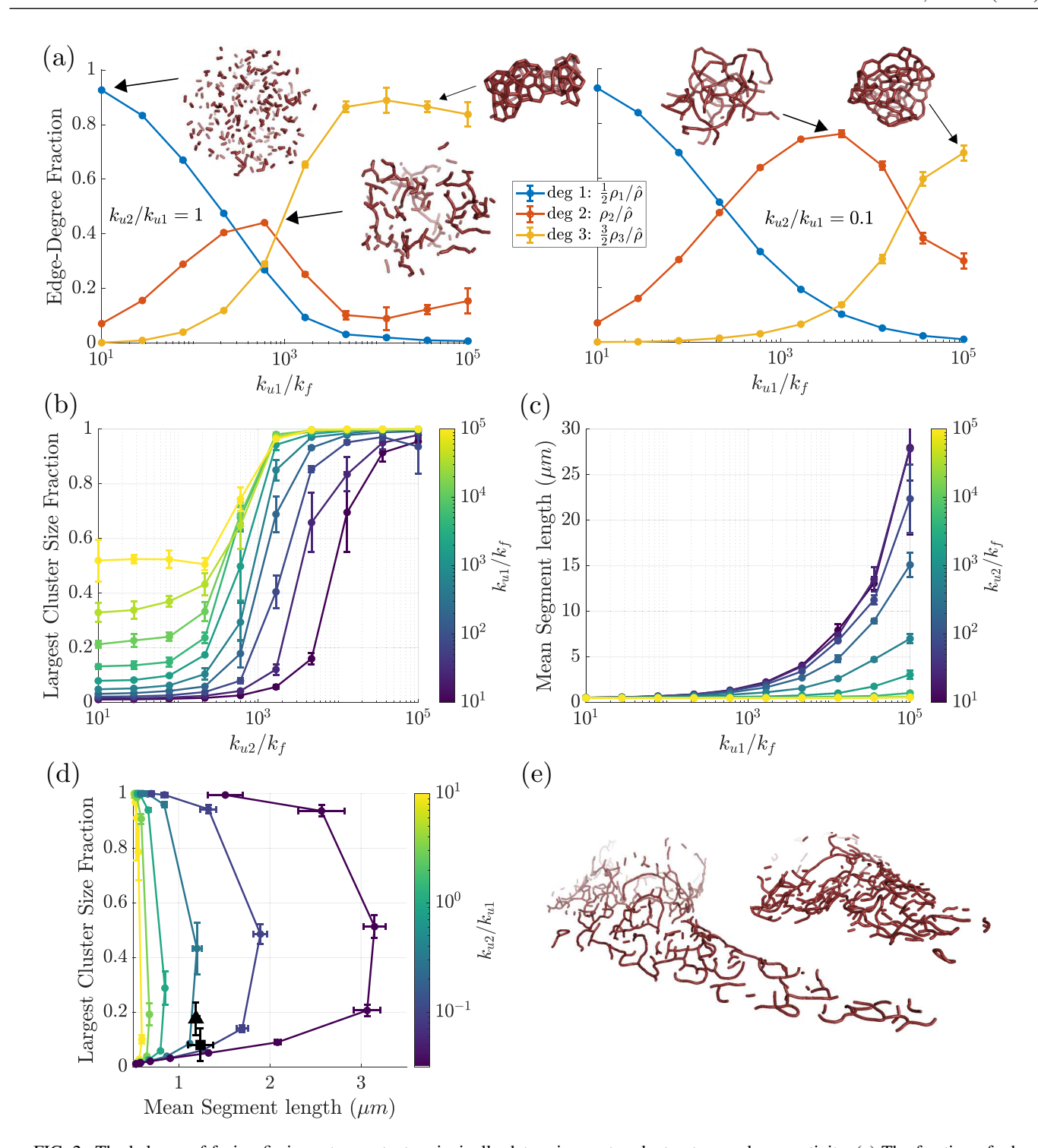


FIG. 2. The balance of fusion-fission rate constants principally determines network structure and connectivity. (a) The fraction of edges connected to nodes of each degree (1-3) in the network is plotted as a function of increasing fusion rate constant. For mapping to dimensional rate units, all simulations use  $k_f = 0.5 \, \mathrm{min}^{-1}$ . Insets show example networks. Left:  $k_{u2} = k_{u1}$ ; right:  $k_{u2} = 0.1 k_{u1}$ . (b) The largest cluster size fraction  $\langle L_G/L \rangle$  is plotted as a function of increasing  $k_{u2}$  for fixed values of  $k_{u1}$  (colors). (c) The mean segment length  $\langle L_{seg} \rangle$  is plotted as a function of increasing  $k_{u1}$  for fixed values of  $k_{u2}$  (colors). (d) Simulated (colored curves) and experimental (black triangle: hiPSC cell [7]; black square: COS-7 cells) networks are plotted in the space of largest cluster size fraction and mean segment length. Colors indicate fixed values of the ratio  $k_{u2}/k_{u1}$  while dots represent specific values of  $k_{u1}$ , which increases from low to high cluster size along each curve. Error bars indicate the standard deviation across simulation trials [(a)–(d)] or experimental images (d). (e) Examples of experimentally derived network structures from a COS-7 cell (left) and a hiPSC cell [7] (right).

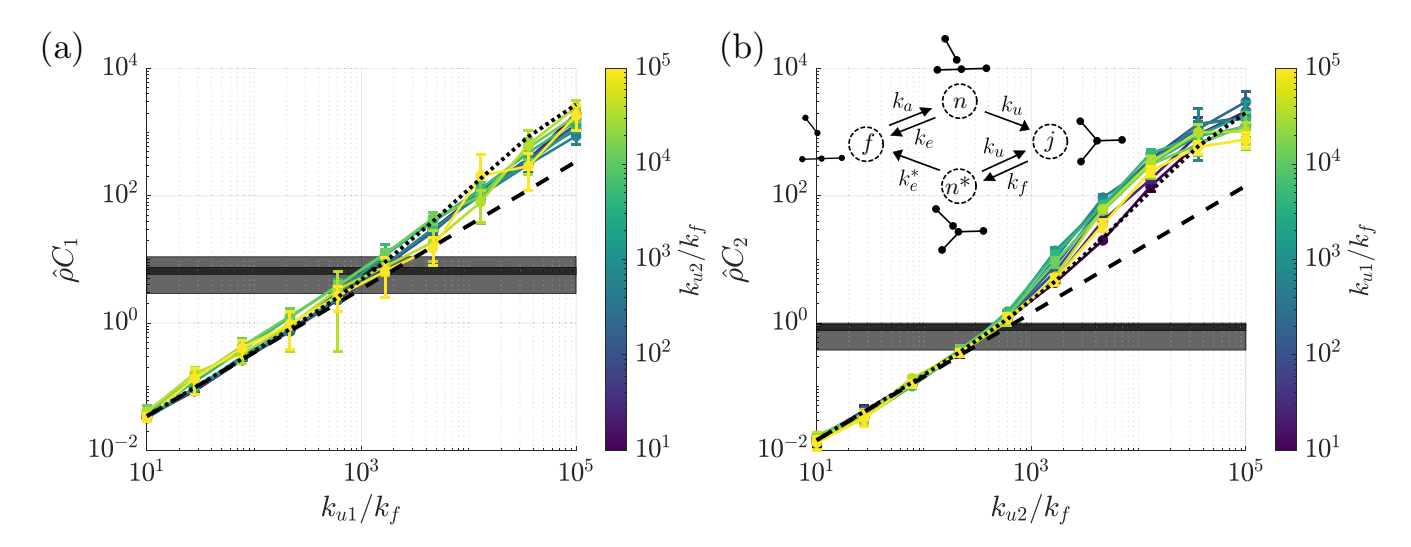


FIG. 3. Mapping local parameters to effective association constants. (a) The tip-tip association constant,  $C_1$ , is plotted as a function of the local fusion rate constant  $k_{u1}$  for different values of  $k_{u2}$  (colored lines). (b) The tip-side association constant,  $C_2$ , is plotted as a function of the local fusion rate constant  $k_{u2}$  for different values of  $k_{u1}$  (colored lines). Inset: a simplified kinetic model approximates the deviation in  $C_2$  from equilibrium at intermediate fusion rate constants. In (a) and (b) dashed lines show the equilibrium mean-field prediction  $(\widetilde{C_i})$ . Dotted lines show predictions from the simplified kinetic model  $(\widehat{C_i})$ . Error bars show standard deviation across simulation trials. Gray boxes show the mean and standard deviation for experimental networks from hiPSC [7] (dark gray) and COS-7 cells (light gray).

by a factor of 100 [29] to  $10\,000 [36]$  when compared to tip-tip fusion.

### B. Spatial constraints and local nonequilibrium kinetics modulate network structure

In order to map from microscopic parameters to large-scale network architecture, we first consider a simplified mean-field model of bulk kinetics. Mass action models have been employed in a wide variety of contexts to determine the behavior of molecular-scale systems from a set of binding and unbinding rates [68–70]. These aspatial models rely on two key assumptions: a well-mixed system (spatially uniform reactant concentrations) and reaction rates that are directly proportional to concentrations. The steady-state concentrations are then found by defining the rate of change for each component and setting the resulting equations to zero.

A mass action model for mitochondrial networks, originally developed by Sukhorukov *et al.* [36], treats nodes of different degree  $(X_1, X_2, X_3)$  as distinct species, undergoing the following reactions:

$$2X_1 \underset{b_1}{\overset{a_1}{\rightleftharpoons}} X_2$$

$$X_1 + X_2 \underset{b_2}{\overset{a_2}{\rightleftharpoons}} X_3, \tag{5}$$

where  $a_1$ ,  $a_2$  represent bulk rate constants for tip-tip fusion and tip-side fusion, and  $b_1$ ,  $b_2$  are the fission rates for degree-2 and degree-3 nodes. These bulk rate constants are effective parameters that depend not only on the microscopic fusion rate constant between a pair of nearby nodes but also on the frequency with which nodes come into contact with each other in an appropriate orientation for fusion to occur.

The steady-state equations expressed in terms of the concentration of nodes  $(\rho_1, \rho_2, \rho_3)$  for degree 1, 2, and 3, respectively) are then given by:

$$\frac{1}{b_1} \frac{d\rho_1}{dt} = -C_2 \rho_1 \rho_2 + \frac{b_2}{b_1} \rho_3 - C_1 \rho_1^2 + 2\rho_2 = 0$$

$$\frac{1}{b_1} \frac{d\rho_3}{dt} = C_2 \rho_1 \rho_2 - \frac{b_2}{b_1} \rho_3 = 0$$

$$\rho_1 + 2\rho_2 + 3\rho_3 = 2\hat{\rho},$$
(6)

where the third equation ensures mass conservation and  $\hat{\rho}$  is the total concentration of edge units in the network.  $C_1 = a_1/b_1$  and  $C_2 = a_2/b_1$  are the effective association constants for the fusion-fission reactions, with dimensions of inverse concentration. These association constants are directly related to the steady-state densities of nodes according to  $C_1 = 2\rho_2/\rho_1^2$ ,  $C_2 = \frac{b_2}{b_1}\rho_3/(\rho_1\rho_2)$ . They are intensive properties of the system, so their values remain constant if the size of the entire system is altered while maintaining the same node densities (see Supplemental Material Fig. S6) [49]. The quantities  $\hat{\rho}C_1$ ,  $\hat{\rho}C_2$  are dimensionless values that describe the overall steady-state balance between fragmentation and connectivity for tip-tip and tip-side fusions, respectively.

As shown in Fig. 3, the simulated association constants for tip-tip and tip-side fusions vary as a function of the corresponding microscopic fusion rate constant. The edge-unit densities and node counts of different degrees can also be directly estimated for experimental data (details under Methods). Comparing these measurements to simulations allows the extraction of individual microscopic fusion to fission parameter ratios that best reproduce observations in live cells. For the two sets of mammalian mitochondrial networks considered here, we estimate  $k_{u1}/k_f = (1400 \pm 200)$ , (1500  $\pm$  700) and  $k_{u2}/k_f = (460 \pm 40)$ , (400  $\pm$  200), giving a similar

ratio  $(k_{u2}/k_{u1})$  to that extracted from measurements of segment length and largest cluster size (Fig. 2).

In our spatially resolved model, fusion between mitochondria can only occur when two nodes are sufficiently close to each other and the connecting edges are favorably oriented. We estimate the effective bulk fusion rate according to  $\widetilde{a}_i = \langle k_{ui}^{\rm eff} \rangle v_{\rm cont}$ , where  $v_{\rm cont}$  is the contact volume surrounding a node and  $\langle k_{ui}^{\rm eff} \rangle$  is the local fusion rate constant averaged over possible edge orientations within the contact volume (see Methods for details). The predicted association constants are then given by  $\widetilde{C}_i = \langle k_{ui}^{\rm eff} \rangle v_{\rm cont}/k_f$ .

The mean-field estimates of the association constants are accurate for low fusion-to-fission parameter ratios, where the networks are largely fragmented. However, at intermediate fusion (near the percolation transition), the observed tip-side association constants scale super-linearly with the fusion rate constant, and at high fusion (fully percolated networks), they flatten out to a sublinear scaling (Fig. 3). Both discrepancies indicate that the mitochondrial network node associations cannot be taken to obey the well-mixed assumptions of bulk kinetics.

Whenever a fission event occurs, the newly distinct nodes are located close to each other and are capable of rapidly refusing before they have a chance to explore the entire domain. For degree-3 nodes in particular, the distribution of edge orientations after fission differs from the distribution when a segment approaches from the bulk. Fission leaves the remaining degree-2 node in a strained, more highly bent state compared to its equilibrium distribution. Further, newly separated nodes are always placed at minimal steric separation,  $2r_s$ , whereas fusion can occur over a range of separations out to the maximal contact separation,  $2r_c$  (see the Supplemental Material for details [49]). Overall, the state of a pair of edges immediately after fission cannot be treated as identical to the state immediately before fusion, breaking the assumptions of the mean-field model.

We can build a simplified kinetic model encompassing this effect by defining a set of discrete states for a pair of nodes [Fig. 3(b), inset]. The f state describes two nodes far apart in the domain, the n state describes the pair within contact range after finding each other from a distance, the  $n^*$  state has the pair within contact range just after a fission, and the j state has the pair joined together into a single node. Notably, the  $n^*$  state tends to favorably align recently separated nodes for refusion, whereas bulk nodes tend to be less-favorably aligned. This system of states contains one-way arrows and thus fails to obey detailed balance [71,72]. So long as the two contact states n and  $n^*$  have different rates of escape to the far f state, the system is not in thermodynamic equilibrium. It should be noted that the biomolecular machinery responsible for mitochondrial fusion and fission consumes GTP [73], and the fission-fusion cycle is thus expected to be a nonequilibrium process. In this sense, the mitochondrial dynamics fundamentally differ from classic molecular clustering systems which have previously been explored with spatial simulations [40,41,66].

Solving for the steady-state probabilities of the abstract model system in Fig. 3(b) inset (see Methods for details) gives the effective association constant  $\hat{C} = \frac{k_{\mu}v_{\text{cont}}}{k_{f}} \frac{p_{\text{esc}}}{p_{\text{esc}}^{p_{\text{esc}}}}$ , where

 $p_{\rm esc}$ ,  $p_{\rm esc}^*$  are the probabilities of escape from the  $n, n^*$  state, respectively, into the f state before fusion. For the mitochondrial dynamics, fission results in two edges within steric contact and in more favorable orientations than would be expected at equilibrium, so that  $p_{\rm esc}^* < p_{\rm esc}$ . The escape probabilities for the two states can be estimated by computing the diffusive escape out of contact range from a spherical shell domain in the presence of a spatially homogeneous reaction rate, as described in the Supplemental Material [49]. The effective association constants,

$$\widehat{C}_{i} = \left(\frac{\langle k_{ui}^{\text{eff}} \rangle v_{\text{cont}}}{k_{f}}\right) \left(\frac{p_{\text{esc},i}}{p_{\text{esc},i}^{*}}\right),\tag{7}$$

approximately match those extracted from simulations for low and intermediate fusion rate constants (Fig. 3).

At low fusion, the escape probabilities approach 1 and the association constants depend linearly on the corresponding microscopic fusion rate constant. At intermediate fusion, the reduced probability of escaping implies likely refusion following each fission event, leading to enhanced association when compared to an equilibrium system.

The effect is most clearly seen for the tip-side association constant  $C_2$  measured near the percolation transition. Here the simplified model approximately matches simulation results in the limit of short segment lengths (low  $k_{u1}$ , purple curve), where the network is partially fragmented into disjoint triskelion structures. Higher values of tip-tip fusion rate constant (green curves) increase the association constant still further, possibly by bringing the danging nodes of nearby triskelions in closer spatial proximity to each other. By contrast, very high values of  $k_{u1}$  (yellow curve) decrease the junction association constant in the intermediate regime, by forming very long linear segments between junctions that greatly slow the ability of dangling ends to find each other.

At very high tip-side fusion rate constants, the system collapses into a fully percolated network. In this regime, there remain a few degree-1 and -2 nodes that cannot access each other without prohibitive deformation of the highly connected network. This results in a saturation of the association constant  $C_2$  at high microscopic  $k_{u2}$ .

For the tip-tip association constant  $C_1$ , there is a smaller deviation from the linear equilibrium behavior. In contrast to the out-of-equilibrium orientation of segments on tip-side fission, a tip-tip fission event places the newly formed segments into an orientational distribution proportional to the fusion rate constant, as expected for detailed balance. The only nonequilibrium effect arises from the close positioning of nodes after fission. At very high rates of the microscopic tip-tip fusion parameter  $k_{u1}$ , mitochondria associate into highly connected, linear structures whose distant peripheral ends are incapable of finding each other within the timescale of the simulation. The association constant thus drops below the values predicted by the approximate model [Eq. (7)].

Our simulations highlight the importance of spatial locality and constraints in determining the steady-state structure of the mitochondrial network. Beyond the fragmented regime, details of the nonequilibrium fission and fusion process can substantially alter the network connectivity away from the mass-action prediction. The mass-action model provides a

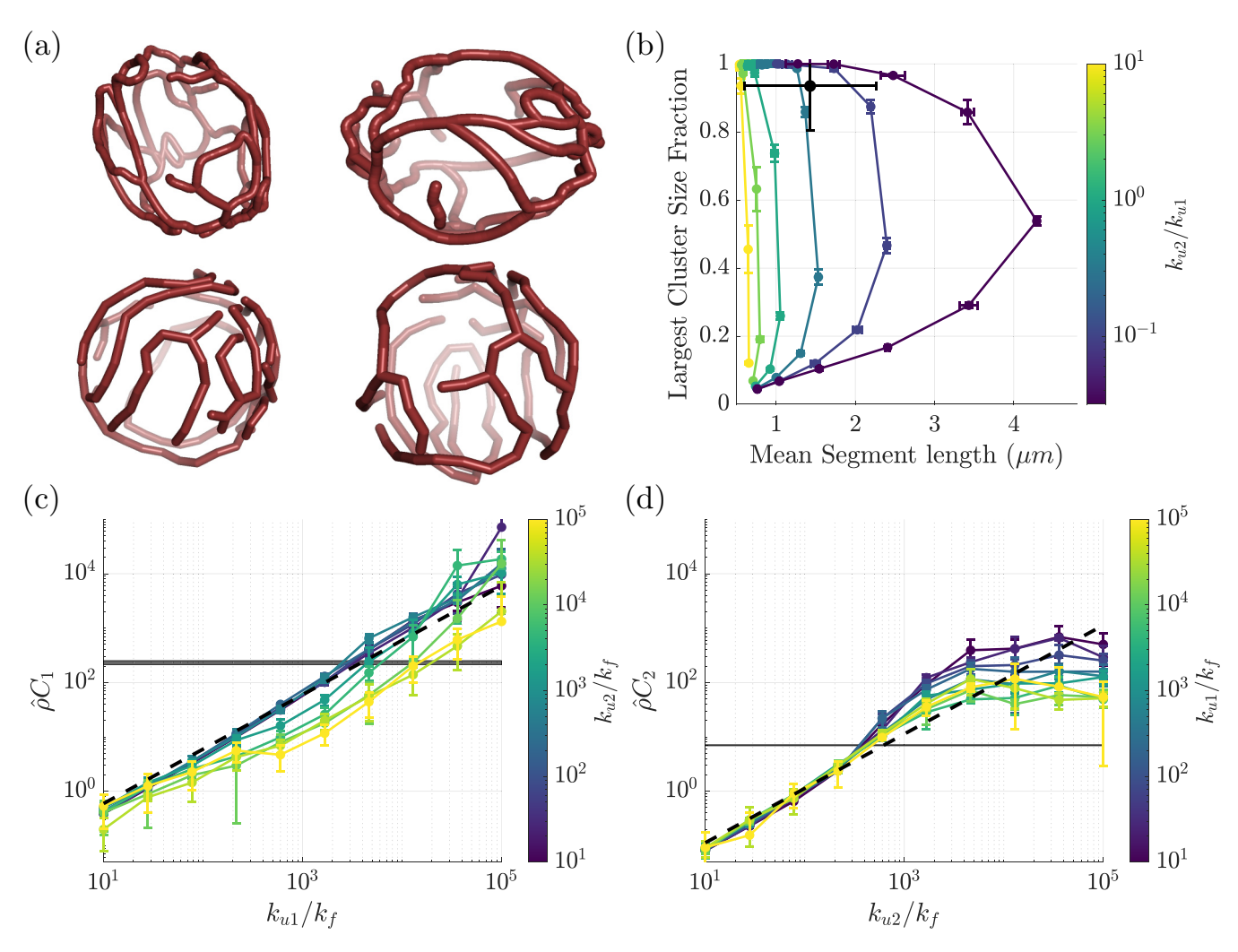


FIG. 4. Structure of surface-bound mitochondrial networks. (a) Example yeast networks obtained from live-cell imaging (top, from Ref. [11]) and via simulation (bottom). (b) The largest cluster size fraction  $\langle L_G/L \rangle$  and mean segment length  $\langle L_{\text{seg}} \rangle$  are plotted for different values of the ratio  $k_{u2}/k_{u1}$  (colored curves). The black point represents the mean and standard deviation of 2794 experimental networks from Ref. [11]. (c) The tip-tip association constant,  $C_1$ , is plotted as a function of the local fusion parameter  $k_{u1}$  for different values of  $k_{u2}$  (colored lines). (d) The tip-side association constant,  $C_2$ , is plotted as a function of the local fusion parameter  $k_{u2}$  for different values of  $k_{u1}$  (colored lines). The black dashed curves show our analytic predictions from the equilibrium mean-field model; gray boxes highlight the mean and standard error of the extracted values from Ref. [11]. Simulations are performed in a spherical cell of radius  $R = 2.3 \, \mu m$ , with total mitochondrial length 60  $\mu$ m to approximate experimentally observed yeast networks. Error bars in (b)–(d) show standard deviation over simulation trials.

useful framework for computing structural metrics of network architecture based on two effective large-scale association parameters  $(C_1, C_2)$  [29,36]. The more detailed spatial model described here goes one step further in estimating these effective parameters from the microscopic fusion and fission rate constants as well as the mechanical properties of the mitochondria.

## C. Surface-bound network architectures exhibit higher connectivity

Our model for mitochondrial network structure can be applied to other cell types and geometries, such as the budding yeast *Saccharomyces cerevisiae*. The mitochondria of these small ( $\sim$ 5 µm in diameter) cells are bound to the inner surface of the cell membrane, so that mitochondrial units are effectively constrained to move on a two-dimensional (2D) shell. Notably, yeast mitochondrial networks are known to

be more highly connected than mammalian networks, well beyond the percolation transition [11]. By incorporating a tethering force into our simulations to hold mitochondria near a spherical boundary, we can generate surface-bound network structures [Fig. 4(a)] and estimate the underlying microscopic parameters that account for the observed network connectivity. The spherical boundary of these effectively 2D surface-bound simulations represents the cell membrane and the total length of mitochondria corresponds to that found in a yeast cell [11].

As in the case of 3D networks, varying the ratio of tip-side versus tip-tip fusion rate constant, as well as the fusion to fission parameter ratios, enables the generation of a family of structures with different mean segment lengths and largest cluster size fractions [Fig. 4(b)]. We extract these two metrics from a previously published database of visualized yeast network structures [11], and compare to the simulation parameter

sweeps. Experimental networks lie in the neighborhood of  $k_{u2}/k_{u1} = 0.28 \pm 0.01$  (mean  $\pm$  standard error), similar to the ratios obtained for 3D networks. This correspondence between microscopic parameter ratios across networks in different cell types suggests that the balance between tip-side and tip-tip fusions is a robust fundamental property of mitochondrial geometry and/or fusion machinery.

As for the 3D mammalian cell networks, we can turn to the simplified aspatial model [Eq. (6)] to map our microscopic parameters to large-scale network structure. In a 2D system, the effective bulk fusion rate becomes a function of the contact area  $a_{\text{cont}}$  rather than the contact volume, and the local fusion rate constant is averaged over the possible 2D edge-unit orientations in this contact area. The node concentrations take on units of 1/area. With these modifications we can write the effective association constants:  $\widetilde{C}_i = \langle k_{ui}^{\text{eff}} \rangle a_{\text{cont}}/k_f$ . As shown in Figs. 4(c) and 4(d), the mean-field approximation matches simulation results in the low-fusion regime. Intermediate and high values of tip-side fusion lead first to enhanced values of  $C_2$  (due to rapid refusion) and then to a flattening below the mean-field prediction (due to mechanical constraints on node accessibility), analogously to the 3D networks. Notably, the saturation at high fusion occurs for values of  $\hat{\rho}C_2$  that are about an order of magnitude lower than in the 3D network structures. This implies that tethering to a surface makes it more difficult for remaining unfused nodes to reach each other, leading to frustrated network structures with limited maximal connectivity.

For any given set of microscopic fusion-to-fission parameter ratios  $k_{ui}/k_f$ , the simulated surface-bound networks are more highly connected (higher  $\hat{\rho}C_i$ ) than their 3D counterparts in Fig. 3. This effect arises from the effectively higher density of nodes when networks are confined to a thin shell next to the cell boundary. Extracting individual parameter values from the empirical yeast network database [Figs. 4(c) and 4(d), gray line] yields  $k_{u1}/k_f = 2400 \pm 100$ ,  $k_{u2}/k_f = 440 \pm 10$ (mean  $\pm$  standard error). These rate constants are only slightly higher than the mammalian cell estimates. When these microscopic fusion rate constants are applied to 3D networks with the appropriate unit-edge density for mammalian cells, they yield values of  $\hat{\rho}C_1 = 12.9 \pm 0.7$  and  $\hat{\rho}C_2 = 0.89 \pm 0.03$ that are approximately consistent with the range observed for mammalian mitochondrial networks [see Figs. 3(a) and 3(b)]. By contrast, the association constants observed in yeast cells are approximately an order of magnitude higher ( $\hat{\rho}C_1$  =  $230 \pm 20$ ,  $\hat{\rho}C_2 = 7.0 \pm 0.2$ ). We therefore conclude that the higher connectivity observed in yeast networks is a result of geometric constraints that confine mitochondria to the cell surface, and the concomitant rise in mitochondrial density at the boundary, rather than substantial alterations in the balance of microscopic fusion-to-fission rate constants.

# D. Mitochondrial flexibility and orientational fusion sensitivity modulate network connectivity

In this model, the angular alignment of mitochondrial units plays two separate roles in determining network structure. First, the bending moduli  $B_1$ ,  $B_2$  control the stiffness of fused degree-2 and degree-3 junctions, respectively. Second, the parameters  $\alpha_1$ ,  $\alpha_2$  set the angular sensitivity of the fusion rate

constant for forming each type of junction. The overall local fusion rate constant scales in proportion to the Boltzmann factor:  $k_{ui}^{\text{eff}} = k_{ui}e^{-\alpha_i f(\Omega)}$ , where  $f(\Omega)$  is a function of the segment orientations, as in Eq. (4). By default, we set  $\alpha_i = B_i/\ell_0 k_b T$ , restricting fusion events to occur only for angular configurations that will give a low mechanical energy following fusion. This choice of angle dependence relates the fusion rate constant for a given edge orientation to the equilibrium probability of that orientation just before a fission event, with direct proportionality between the two for degree-2 junctions. Removing the angle dependence for fusion rate constants would lead to prohibitively high bending energies just after a fusion event. Making the dependence much stricter would cause out-of-equilibrium network fragmentation as fission at a node would often lead to configurations where local fusion is impossible.

Given the role of the angular sensitivity in the fusion rate constant, increasing  $\alpha_i, B_i$  in tandem at both degree-2 and degree-3 junctions exponentially decreases the overall association constants at a fixed value of the local fusion prefactor  $k_{ui}$ [Figs. 5(a) and 5(b)]. As an alternate approach, we isolate the effect of junction stiffness on the mechanics of the network, varying the bending modulus,  $B_i$ , while maintaining a fixed  $\alpha_i$ in defining the fusion rate constant. The effect on the association constants is then nonmonotonic [Figs. 5(c) and 5(d)]. At low fusion rate constants, the bending stiffness has no effect as the network structure depends on the equilibrium balance between fusion and fission. At intermediate fusion, near the percolation transition, increasing the bending modulus raises the network connectivity (higher  $C_1, C_2$ ). This effect arises due to the out-of-equilibrium local fusion and fission interactions. High junction stiffness implies that after fission the edge orientations are very tightly constrained to the optimal values that give the highest local fusion rate constant. As a result, rapid refusion is very likely and the escape probability is low, giving a notably superlinear increase in association constant as a function of  $k_{ui}$ . At the highest fusion rate constants, when the network is compact and thoroughly interconnected, high bending stiffness constrains the remaining dangling degree-1 and degree-2 nodes from being able to reach each other, reducing the overall association constants  $C_i$  [Figs. 5(c) and 5(d)].

Overall, increasing the mechanical stiffness of the mitochondrial segments and junctions can reduce network connectivity (by limiting the configurations for which fusion can occur) or enhance it (by increasing the probability of being in a favorable configuration following fission to enable rapid refusion). The dominant effect is determined by the microscopic kinetics of how fusion rate constants depend on the orientations of mitochondrial units.

## E. Mitochondrial motility hinders percolation but enhances maximal network connectivity

We next consider the role of effectively diffusive mitochondrial motion in modulating simulated network architectures. A variety of recent measurements in both eukaryotic and prokaryotic cells have demonstrated that apparent diffusion in the cytoplasm actually relies on active processes within the cell, and is substantially reduced by ATP depletion [10,74,75] or inhibition of various molecular motors [10,76,77]. We

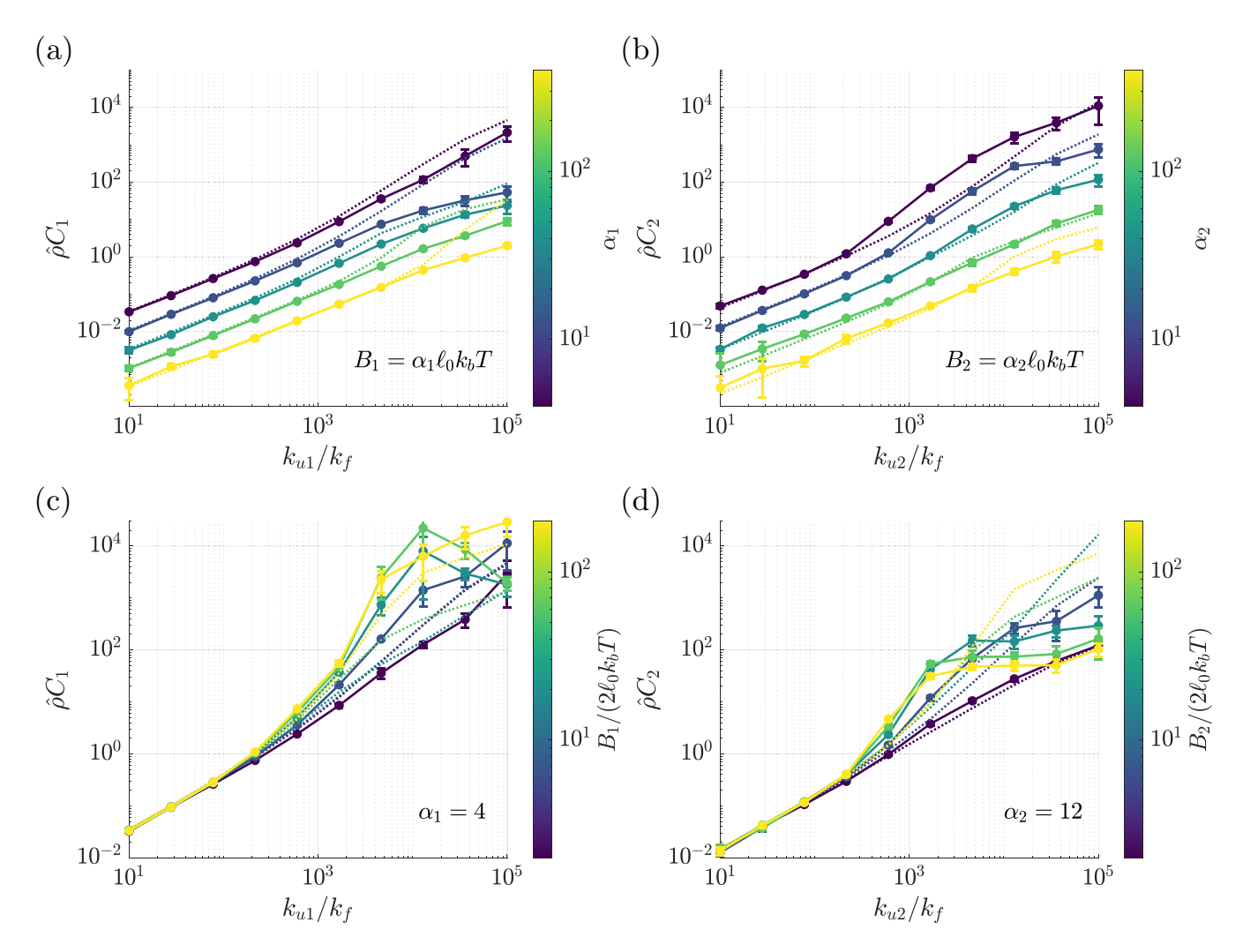


FIG. 5. Effect of fusion sensitivity and bending stiffness on network structure. (a)  $C_1$  is plotted as a function of the local fusion parameter  $k_{u1}$  for different values of  $B_1$ ,  $\alpha_1$  (colored lines). (b)  $C_2$  is plotted as a function of the local fusion parameter  $k_{u2}$  for different values of  $B_2$ ,  $\alpha_2$  (colored lines). (c)  $C_1$  is plotted as a function of the local fusion parameter  $k_{u1}$  for different values of the bending modulus  $B_1$  (colored lines), while  $\alpha_1 = 4$  is held constant. (d)  $C_2$  is plotted as a function of the local fusion parameter  $k_{u2}$  for different values of the bending modulus  $B_2$  (colored lines), while  $\alpha_2 = 12$  is held constant. Dotted curves indicate the approximate nonequilibrium association constants estimated from Eq. (7), for each parameter set. All panels use a constant ratio of  $k_{u2}/k_{u1} = 0.3$ . Error bars indicate standard deviation across simulation trials.

therefore consider the diffusive motion in our model to be an emergent result of many unspecified spatially distributed active processes.

To investigate the effect of active diffusion on network architecture, we alter the temperature T that sets the magnitude of the stochastic Brownian forces  $\vec{F}^{(B)}$ , without changing the angle-dependence parameter  $\alpha_i$  in the fusion rate constants. The effective diffusivity of mitochondrial units is measured by tracking the ensemble-averaged mean-squared displacement  $\langle x^2(t) \rangle$  of the center-of-mass of each unit over short times  $(\Delta t \leq 1)$  and setting the slope of this curve equal to  $6D_{\rm eff}t$ . As expected, lowering the temperature at a fixed fusion rate constant proportionally decreases the effective diffusivity of mitochondrial units [Fig. 6(a)]. Increasing fusion drives down the edge diffusivity, as each mitochondrion becomes more likely to be incorporated into larger network components. The diffusivity drops very low above the network percolation transition, where most edges are incorporated into a single large cluster [see Fig. 2(b)].

In terms of network structure, decreasing the mitochondrial motion has an analogous effect to increasing the mechanical stiffness of the network. Indeed, lower effective temperature is expected to yield a tighter distribution of bending angles at fused nodes. As a result, in highly percolated networks, lower temperature reduces the large-scale network flexibility and thus limits the ability of peripheral lowerdegree nodes to reach each other, reducing association constants [Figs. 6(b) and 6(c)]. For intermediate fusion rate constants, lower temperature results in more favorable edge orientations immediately after fission. This makes refusion events more likely to occur before the two nodes can escape from contact, resulting in a higher association constant. This effect is further enhanced by the slower motion of edges after a fission event, which also lowers the escape probability. The resulting association constants at low to intermediate fusion rate constants can be approximately predicted from the simplified model encompassed by Eq. (7) [Figs. 6(b) and 6(c), dotted lines].

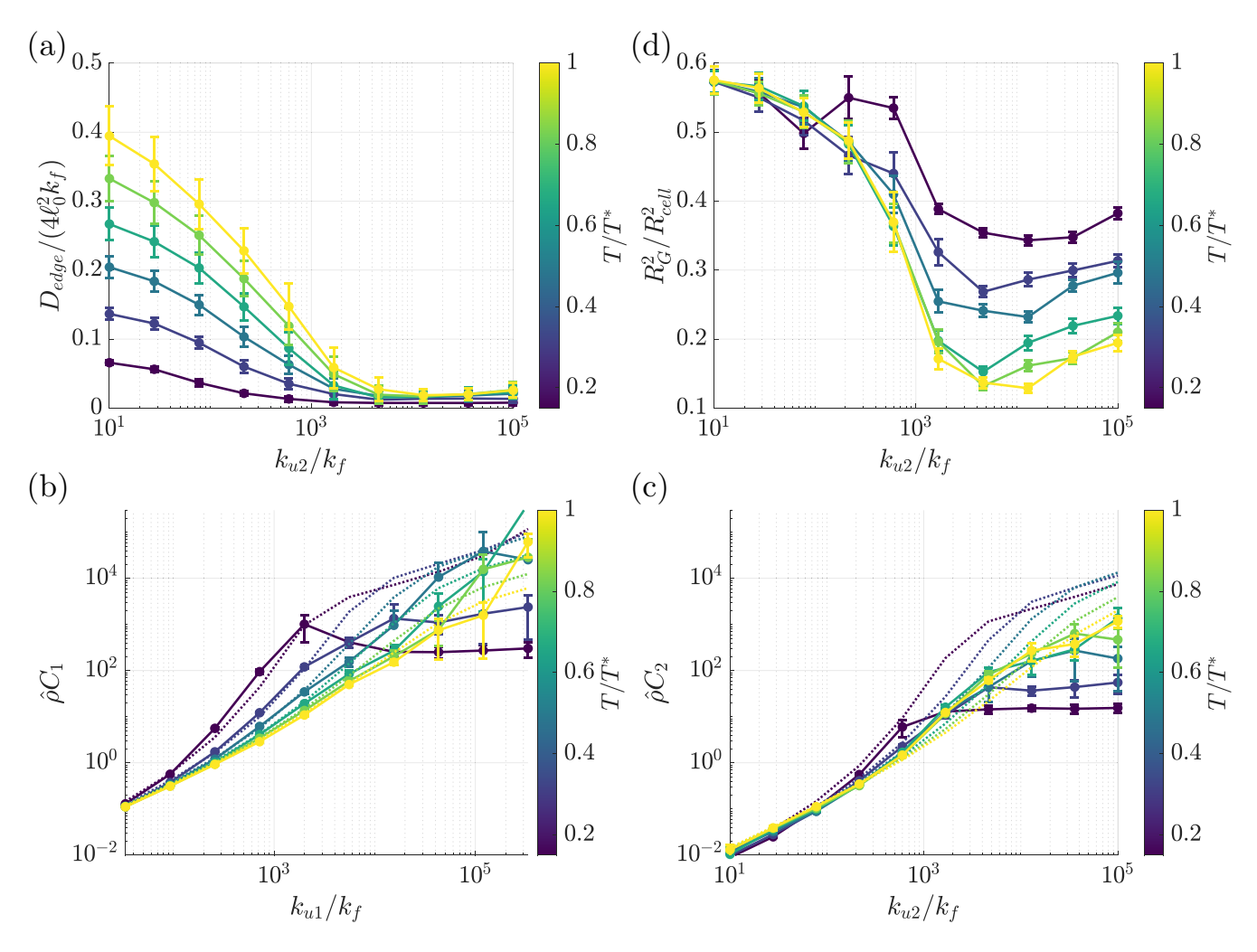


FIG. 6. Mobility affects network structure. (a) The effective edge diffusivity  $D_{\text{edge}}$  is plotted as a function of  $k_{u2}$  for different values of the diffusion temperature,  $k_bT$  (colored lines) relative to the default diffusion temperature, denoted  $T^*$ . (b) The tip-tip association constant,  $C_1$  is plotted as a function of  $k_{u1}$  for different values of the diffusion temperature,  $k_bT$  (colored lines). (c) The tip-side association constant,  $C_2$  is plotted as a function of  $k_{u2}$  for different values of the diffusion temperature,  $k_bT$  (colored lines). Dotted lines indicate (nonequilibrium) analytic predictions. (d) The radius of gyration  $R_G$  is plotted as a function of  $k_{u2}$  for different values of the diffusion temperature,  $k_bT$  (colored lines). Highly fused networks are more compact, but this effect is reduced at lower temperatures, where mitochondria are less mobile and the remodeling process freezes up. Panels (a)–(d) use  $k_{u2}/k_{u1} = 0.3$ . Error bars indicate standard deviation across simulation trials.

Finally, the magnitude of active diffusion is found to affect the network compactness. At intermediate to high fusion and lower effective temperature, the reduced mobility and flexibility described above lead to increased concentrations of degree-2 nodes, longer segment length, and therefore higher radius of gyration,  $R_G$  [Fig. 6(d)]. Higher effective temperature allows for greater flexibility, catalyzing the rearrangements necessary to bring the network to a highly compact state (small  $R_G$ ). Analogous effects have previously been noted for the formation of diffusion-limited aggregates by particles with varying diffusive step sizes [47].

### F. Rapid network rearrangement requires intermediate fusion rate constants

To gain a sense of the overall rearrangement dynamics of mitochondrial networks, we quantify the rate of tip-tip and tip-side novel fusion in our simulations, defined as the total number of fusion events of each type per unit time that do not involve the connected partner prior to fission. The measured rates of novel fusion show a nonmonotonic dependence on the microscopic fusion rate constants  $k_{ui}$  [Figs. 7(a) and 7(b)]. At low  $k_{ui}$  all fusion events are rare, whereas at high  $k_{ui}$  the escape probability following a fission event is low and most fissions thus lead to a rapid refusion with the same mitochondrial partner. At high network connectivity, mechanical and spatial constraints prevent distant nodes from reaching each other, so that any fissing pair is very likely to refuse rather than seeking out a novel fusion partner. The novel fusion rates peak at intermediate  $k_{ui}$ , where contacts between nearby nodes tend to result in successful fusion but escape from the contact volume following fission is still frequent. Interestingly, the extracted microscopic fusion rate constants for mammalian mitochondrial networks lie reasonably close to the values that yield peak novel fusions. This observation indicates that mammalian mitochondrial networks are not only poised at the boundary of structural percolation, but are also located in a parameter regime that gives high dynamic turnover rates of

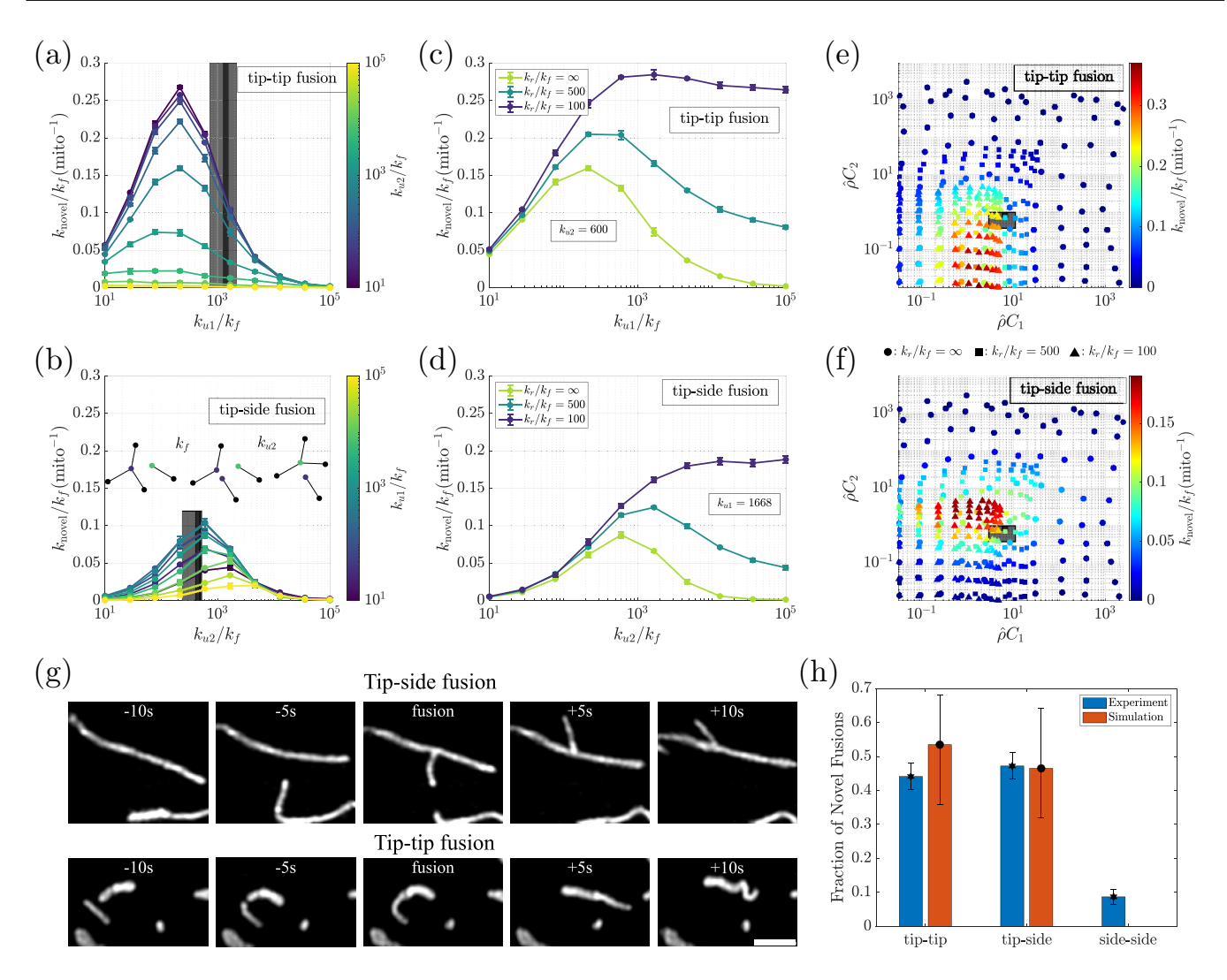


FIG. 7. Novel fusions peak at intermediate fusion rate constants. [(a) and (b)] The rate of novel fusions of each type is plotted as a function of the fusion parameter  $k_{u1}(k_{u2})$  for different values of the fusion parameter  $k_{u2}(k_{u1})$  (colored lines). Nodes do not enter an inactive state following fission and may immediately refuse. Vertical gray bars indicate the range of  $k_{u1}(k_{u2})$  extracted from experimental networks. Inset: A degree-3 node (purple) undergoes a fission event followed by tip-side novel fusion with a degree-1 node (green). [(c) and (d)] The rate of novel fusions of each type is plotted as a function of the fusion parameter  $k_{u1}(k_{u2})$  for different values of the recharge rate,  $k_r$  and fixed  $k_{u2}(k_{u1})$  corresponding to the experimentally relevant regime. Nodes enter an inactive state following fission, returning to an active state (in which fusion is allowed) at rate  $k_r$ . [(e) and (f)] The rate of novel fusions of each type is plotted (colors) as a function of the mean-field association constants,  $\hat{\rho}C_i$ . Symbol shape corresponds to different values of the recharge rate,  $k_r$ . Gray boxes show the experimental values (mean and standard deviation) of  $\hat{\rho}C_i$  for hiPSC [6] (dark gray) and COS-7 cells (light gray). (g) Examples of observed fusion events between mitochondria in COS-7 cells. Top: tip-side fusion. Bottom: tip-tip fusion. Scale bar: 2 µm. (h) The fraction of fusion events of each type observed in COS-7 cell imaging (blue) and extracted from simulations (red). Error bars: [(a)–(d)] standard deviation across trials; (h) for experimental measurements: sampling error for a binomial distribution; for simulations: error bars show range of results corresponding to parameters for the light gray box in (e) and (f).

the network, allowing each mitochondrion to sample different fusion partners relatively rapidly.

We note that the predicted novel fusion rates  $k_{\text{novel}}$  are expected to correspond to the observed fusion rates reported in the literature (i.e., the frequency of observed fusion events per unit time per mitochondrial quantity), providing a link between microscopic kinetics and observed rearrangement rates. Given our default simulation timescale set by  $k_f = 0.5 \text{ min}^{-1}$ , the total rate of novel fusions (using mammalian cell estimates of  $\hat{\rho}C_1$ ,  $\hat{\rho}C_2$ , see Fig. 3 gray boxes) is estimated to be  $0.05-0.12 \text{ min}^{-1}$  per mitochondrial unit. These values

are comparable with the measured rate of  $\sim$ 4 fusion events per hour per mitochondrion reported for mammalian cells in Ref. [60]. This steady-state novel fusion rate corresponds to a characteristic time for a "complete" fission (a fission event that does not result in refusion with the same partner) of  $\sim$ 12 min, in agreement with the fission timescales of 10–20 min used in prior studies [9,37,62,63]. Recently published time-lapse data of mitochondrial network dynamics in hiPSC cells and accompanying network-tracking software [7] yields an estimate of 0.24–0.32 fusion or fission events per minute per  $\mu$ m of mitochondrial length, also comparable with the

simulated values shown here. The matching timescales for novel fusion justify our selection of the microscopic fission rate constant, and enable the dimensionless results of the model to be interpreted in terms of concrete time units.

Interestingly, imaging of mitochondrial dynamics indicates that mitochondria do not tend to refuse immediately following a visible fission event [2,60]. We note that it is possible that rapid fission and refusion cycles do occur but cannot be observed given the limited spatiotemporal resolution of the imaging studies. In this case, the observable fissions and fusions would correspond to the complete fissions and novel fusions of our simulation model. An alternate explanation for the absence of rapid refusion in imaging studies is that there is an inherent delay before recently divided mitochondria are able to acquire the machinery necessary for fusion. We therefore consider an extension of the model that prevents immediate refusion by incorporating a "recharge rate,"  $k_r$ . When nodes undergo fission, they enter an inactive state in which they cannot undergo fusion (i.e.,  $k_{ui} \rightarrow 0$  for each inactive node). Nodes in the inactive state then return to the active, fusion-capable, state with rate  $k_r$ . The simulations described thus far correspond to instantaneous reactivation, with  $k_r \to \infty$ .

Slow recharge rates allow newly divided nodes to escape from their original partner before refusing. The separation of two newly divided nodes to outside their contact range requires an average of roughly  $\tau_{\rm esc}\approx 0.0024$  (see Supplemental Material [49]), indicating that dimensionless recharge rates with  $k_r\lesssim 400$  are sufficient to enable nodes to leave the immediate vicinity of their previous fusion partner. Slower recharge rates yield an enhancement in novel fusions when  $k_{ui}$  are high [Figs. 7(c) and 7(d)]. However, at low values of microscopic fusion rate constant  $k_{ui}$ , slow recharge can lower the overall rate of fusion (novel and refusions both), causing the networks to become less well connected.

As shown in Figs. 7(e) and 7(f), the peak novel fusion rates occur at intermediate values of the association constants. Although slower recharge boosts the peak rate of novel fusions, the overall dependence on the association constants is the same for a broad range of recharge rates. Specifically, the maximum rate of novel fusion occurs when  $\hat{\rho}C_1$ ,  $\hat{\rho}C_2\approx 1$ , corresponding to a system where the fusion and fission are closely balanced. The experimentally extracted association constants for mammalian networks are  $\hat{\rho}C_1=6.6\pm0.9$ ,  $7\pm4$  and  $\hat{\rho}C_2=0.9\pm0.1$ ,  $0.7\pm0.3$ , which gives novel fusion rates that are approximately 60% of the maximum possible values. Notably, these values of  $\hat{\rho}C_1$  cannot be reached with a recharge rate of  $k_r \leqslant 100$ , setting a lower limit on the rate at which mitochondria are able to recover and engage in subsequent fusion events.

The predicted rates of tip-tip versus tip-side novel fusions are comparable  $(0.05 \pm 0.02, 0.04 \pm 0.01 \, \mathrm{mito^{-1} \, min^{-1}}, \, \mathrm{respectively},$  based on measured association constants for COS7 cells), as previously reported for mitochondrial dynamics in mammalian cells [60]. To further test this prediction, we perform an analysis of fusion events via live imaging of the mitochondrial networks in COS-7 cells. Our ability to quantify fusion rates is limited by the impracticality of reliably identifying all fusion events within a dense population of mitochondria in the three-dimensional mammalian cytoplasm.

Thus, we do not report absolute frequencies of fusion. Instead, we manually select well-resolved events characterized by prolonged contact between mitochondria and categorize them as tip-tip, tip-side, or (rarely) side-side fusions [Fig. 7(g)]. Notably, the identified events may or may not involve exchange of mitochondrial material, which is not measured here. Given that our model describes structural rearrangements of the network, the corresponding experimental measurements provide information on the formation of new structural connections between mitochondria in different orientations. We find that roughly 44% of 161 observed apparent fusions are tip-tip, while 47% are tip-side, in good agreement with the extracted simulation-based novel fusion rates [Fig. 7(h)]. This near-equivalence of novel fusions for the two event types is observed even though the microscopic fusion rate constants  $(k_{u1}, k_{u2})$  differ by a factor of 3. The distinction arises because the novel fusion rate incorporates geometric and mechanical constraints that affect the distribution of angle-dependent fusion rate constants as well as the ability of newly divided nodes to escape from each other.

Overall, our results show that mammalian mitochondrial networks lie in a parameter regime that enables them to be highly "social" [78,79], rapidly encountering novel partners for both tip-tip and tip-side fusions.

#### IV. CONCLUSIONS

The modeling and simulation results described here form a framework for understanding how cell-scale mitochondrial network structure arises from the dynamics of individual organelle units. Mitochondrial networks vary widely, from "social" networks of interacting but physically fragmented units [78,79] to highly connected tubular networks [11,29,80], depending on cell type, genetic perturbations, and environmental conditions. The spatially resolved model presented here elucidates the impact of underlying microscopic rate constants and mechanical features on the morphology of these networks.

The network architecture is shown to be highly dependent on the ratio of microscopic fusion and fission rate constants for tip-tip and tip-side interactions. Analysis of published data for both mammalian and yeast cell networks indicates that the two microscopic fusion rate constants are relatively well balanced  $(k_{u2}/k_{u1} \approx 0.3)$ , resulting in structures with modest segment lengths. While mammalian networks are poised at the edge of the percolation connectivity transition, yeast networks are generally highly connected structures. Our simulations demonstrate that this distinction can arise from geometric confinement and the effectively high density of mitochondria at the surface of the yeast cell, without requiring substantially different microscopic rate constants. This theoretical result gives rise to a testable prediction that could be pursued through future experimental efforts. Namely, it implies that decoupling yeast mitochondria from the cell cortex by knocking down tethering factors should result in partial fragmentation of the network.

Using a mass-action model, we show that the effective mean-field association constants  $(C_1, C_2)$  that describe network architecture [36] can be analytically predicted from microscopic parameters and geometric constraints. Going

beyond prior work that linked network structure with the global balance of fusion and fission [6,29,36], these results enable a deeper mechanistic understanding of how global structure arises from individual organelle interactions.

Crucially, the standard mass-action model breaks down at intermediate to high fusion rate constants, where spatial transport becomes limiting. For intermediate rate constants there is an enhancement in the probability of rapid refusion following each fission event, due to the fact that recently divided edges are prealigned to facilitate fusion. This is a nonequilibrium feature, resulting in a superlinear dependence of association constants on microscopic fusion to fission parameter ratios. The model thus serves as an example of the general principle that an input of energy into a biomolecular system can amplify specific states [81] and sharpen the system's response to small parameter changes [82,83].

At high fusion, the formation of spatially extended structures precludes the ability of dangling ends to find each other, resulting in a plateau of the association constants. The mechanical flexibility of mitochondrial junctions, as well as the motility of mitochondrial units, both suppress refusion at intermediate  $k_{ui}$  and increase the maximal network connectivity at high  $k_{ui}$ .

We further quantify the rate of novel fusions in the simulated networks, wherein a mitochondrial unit switches to another fusion partner, rather than refusing rapidly with the same partner after a fission event. Such novel fusion rates provide a metric for network rearrangement timescales, and are maximized at intermediate values of the microscopic fusion rate constant, somewhat below the percolation transition. Mammalian mitochondrial networks are shown to operate in a parameter regime with relatively high rates of novel fusion, allowing for constant rearrangement of network structures. Thus, mammalian mitochondria can be thought of as highly "social" organelles [78,79], with frequent interactions and exchanges between distinct segments.

We note that in experimental studies mitochondria are generally not observed to fuse again immediately after fission [60]. However, the spatiotemporal resolution of 3D imaging is inherently limited (usually with frame rates below 10 Hz), so that rapid fission and refusion events may still occur without being directly observable. Such rapid refusion could be supported by the convergence of fusion and fission machinery at ER-mitochondrial contact sites, enabling fast successive dynamics [84]. In this case, the "novel fusion" and corresponding "complete fission" rates predicted by our simulations (rather than the microscopic fusion and fission rate constants) are more directly comparable to experimental measurements. Alternately, there may be additional transitions that must occur before a newly divided mitochondrion is capable of fusing again, explicitly precluding rapid refusion events. We thus incorporate into our model a latent recovery period, which enhances the rate of novel fusions at high values of  $k_{ui}$ , but also limits the overall association constants and hence the connectivity of the network. Regardless of the microscopic fusion and recovery kinetics, the rate of novel fusion is shown to be maximized at intermediate association constants ( $\hat{\rho}C_i \approx 1$ ), where overall fusion and fission rates are approximately balanced. Further, the association constants obtained for mammalian cells are shown to correspond to approximately equal rates of novel tip-tip and tip-side fusions, as observed in live-cell imaging measurements.

Prior works have employed a number of methods for quantifying mitochondrial fusion rates. Motivated by the putative function of fusion in mixing mitochondrial material, a common experimental method involves activating photoactivatable green fluorescent protein (PA-GFP) (or photobleaching a fluorescent protein) in a region of interest, then measuring spreading of the signal. This approach allows a characterization of content mixing through the population of mitochondria, without yielding an explicit measurement of the fusion rate itself [6,85–87]. Other approaches rely on observing fusion events of individual mitochondria labeled with PA-GFP [86,87]. However, overall fusion rates are generally not reported when these studies are carried out in compact cell types where mitochondria are densely packed in a 3D cytoplasm. In this work we report the relative frequencies of different types of structural rearrangements associated with mitochondria joining in a tip-tip and tip-side manner. The observed events do not necessarily involve the exchange of mitochondrial contents, nor do we identify the complete set of fusion events in the dense mitochondrial population. This is appropriate, since we focus on the impact of fusion and fission on network architecture. The experimental measurements reported here indicate that tip-tip and tip-side fusions occur with similar frequencies, as predicted by the computational model.

A key advantage of our modeling approach is that it enables appropriate microscopic rate constants to be extracted from observations of the steady-state structure and large-scale dynamics of the network. Imaging modalities such as lattice-light sheet and scanning confocal microscopy make it possible to extract three-dimensional architectures of mitochondrial networks, while recent advances in image processing enable the construction of temporal trajectories for the networks [7]. Future experimental work will further elucidate how these structures and trajectories vary in response to environmental, pharmacological, and genetic perturbations. Experimental perturbations that alter global mitochondrial dynamics [11,21,29] may do so through a combination of modulating fusion and fission rate constants, mitochondrial flexibility, and transport. Comparison of the resulting data to the spatially resolved models described here will enable a quantitative understanding of what changes in microscopic parameters underlie the observed cellular-scale alterations in structure and global dynamics.

This model sets the stage for addressing a number of open questions concerning dynamics on and of the mitochondrial network. First, how does network morphology control and affect the distribution and dispersion of proteins, nucleoids, ions, and lipids within the mitochondrial compartments? The spatiotemporally resolved simulations form a natural platform for tracking the spread of intramitochondrial material. In upcoming future work, we aim to leverage the framework presented here to characterize how the rate of material spreading through mitochondrial networks is determined by local fusion, fission, and transport kinetics. Second, how efficiently can mitochondria be sorted, during cell division or through quality control mechanisms, based on their connectivity and material contents? Sorting of healthy mitochondria into daughter buds has been proposed as a mechanism contributing

to the aging of budding yeast cells [88]. Selective destruction of unhealthy mitochondria excluded from the network structure is also thought to be a major component of mitochondrial homeostasis [2,89] and could be incorporated into the model. Third, the spatial architecture of the mitochondrial network may modulate the distribution of interactions with other cellular structures, including the localization of ribosomes to the mitochondrial surface [90] and the formation of contact sites between mitochondria and the endoplasmic reticulum [91]. Understanding the connectivity and transport of mitochondria could elucidate how such contacts are maintained and how they respond to changing conditions. Finally, a number of studies have highlighted the interplay between cellular metabolism and the structural state of mitochondrial networks [4,6,14,33]. Investigating the energetic cost of fusion and fission, as well as the benefits to overall ATP production associated with network remodeling, is an important target for future work.

Overall, our simulations provide an *in silico* framework for exploring the interplay of structure and dynamics in the mitochondrial population, furthering our understanding of how the observed morphology of these organelles couples to their many biological functions.

#### V. METHODS

Simulation code for dynamic mitochondrial networks, written in Fortran and Matlab [92] is provided on GitHub [93].

### A. Mechanical and dynamic model for the mitochondrial network

#### 1. Mitochondrial mechanics

Individual mitochondrial units are represented as edges of ground-state length  $\ell_0=0.5~\mu m$  and steric radius  $r_s=0.1~\mu m$ . When the units are connected into larger structures, nodes of degree 2 and 3 mark the connection points. Whenever an edge terminates at a degree 1 node, the node is placed at an inset distance of  $r_s$  along the length of the edge. The length of the edge ( $\ell$ ) is then defined to extend to the tip of the surrounding steric spherocylinder, so that the ground-state value of this length remains at  $\ell_0$  regardless of the edge connectivity.

The time evolution of the nodes is governed by an overdamped Langevin equation Eq. (1), incorporating mechanical forces associated with bending, stretching, steric interaction, and confinement energies for the edge configurations. The mechanical model is analogous to that commonly used for simulating bead-rod chains at the macromolecular scale [58,94]. The stretching energy for each individual unit is set to

$$E_{i,\text{stretch}} = \frac{1}{2} \frac{K_{\text{stretch}}}{\ell_0} (\ell_i - \ell_0)^2, \tag{8}$$

where  $\ell_i$  is the length of edge i, and  $K_{\text{stretch}}$  is the stretching spring constant, set sufficiently high that the root-mean-squared (rms) deviation in edge length is below  $0.05\ell_0$ .

The bending energy at each junction node is given by Eq. (3) and depends on the angles between edges connected at that junction. For a degree-2 node,  $\theta_i$  is the angle between the two edges and the bending energy is lowest at  $\theta_i = 0$ . For a degree-3 junction, the three angles  $\theta_i^{(j)}$  between the

adjacent edges minimize the bending energy in a symmetric planar configuration with  $\theta_i^{(j)} = 60^\circ$ . The bending moduli  $B_1$ ,  $B_2$  scale the energetic penalty for deviating away from the ground-state angles, and their default magnitude is estimated from experimental data as described in the Supplemental Material [49].

A steric energy  $E_{i,j,\text{steric}}$  is defined for each pair of edges i, j that are not directly connected to each other. We compute the minimal distance  $d_{i,j}$  between the line segment connecting the nodes of edge i and the line segment connecting the nodes of edge j. The steric energy is set to give a quadratic penalty when this minimal distance is less than twice the steric radius:

$$E_{i,j\text{steric}} = \begin{cases} \frac{1}{2} K_{\text{steric}} (d_{i,j} - 2r_s)^2, & \text{if } d_{i,j} < 2r_s \\ 0, & \text{otherwise,} \end{cases}$$
(9)

where the steric modulus  $K_{\text{steric}}$  is set sufficiently high that the rms value of  $|d_{i,j}-2r_s|$  for sterically interacting edges is less than  $0.02\ell_0$ . This form of the steric energy effectively treats individual fragmented units as spherocylinders of radius  $r_s$  and total length (to the tips of the spherical caps) equal to  $\ell_0$ . Edges connected into longer tubes overlap their hemispherical end-caps so that the nonconnected mitochondria are excluded from a continuous region of radius  $r_s$  surrounding the entire tube.

The final mechanical component of the model is the confinement force. Simulations are carried out in a spherical domain of radius  $R_{\text{cell}} = 10\ell_0$ , with a steep quadratic energy penalty for mitochondrial nodes that step outside the domain. For surface-bound simulations representing yeast mitochondria, we use  $R_{\text{cell}} = 4.6\ell_0$  and an additional hookean confinement force provides a tethering of the mitochondria to the inside surface of the domain. The confinement energy is thus defined for each node i:

$$E_{i,\text{conf}} = \begin{cases} \frac{1}{2} K_{\text{conf}}(|\vec{r}_i| - R_{\text{cell}})^2, & |\vec{r}_i| > R_{\text{cell}} \\ \frac{1}{2} K_{\text{tether}}(R_{\text{cell}} - |\vec{r}_i|)^2, & |\vec{r}_i| < R_{\text{cell}}, \text{ (tethered)} \\ 0, & \text{otherwise} \end{cases}$$

All 3D mitochondrial network simulations include  $\hat{\rho}V = 250$  edge units in the spherical domain. All surface-bound simulations include  $\hat{\rho}V = 120$  edge units, giving a similar volume density to that found in mammalian cells and yeast cells, respectively.

### 2. Network dynamics

At each step of the simulation, the total mechanical energy for all nodes and edges is computed, and the mechanical force  $\vec{F}^{(\text{mech})}$  is found as the spatial derivative of that energy with respect to node positions [Eq. (2)]. In addition, the Brownian force is computed as  $\vec{F}^{(B)} = \vec{\eta} \sqrt{2k_bT\mu/\Delta t}$  with  $\Delta t$  the simulation timetep,  $\mu$  the friction coefficient of each node,  $k_bT$  the effective thermal energy, and each dimension of  $\vec{\eta}$  a normally distributed random variable with zero mean and unit variance. We nondimensionalize length units by  $2\ell_0$ , time units by  $1/k_f$ , and force units by  $\mu$ . The default effective thermal energy is set to  $k_bT=1$  in these dimensionless units. The simulations are integrated forward using a fourth-order Runge-Kutta method [95] (previously validated for Brownian

dynamics simulations [96]) to update the node positions with time step  $\Delta t = 10^{-4}$ .

At each time step of the simulation, a pair of nodes is able to undergo fusion if they are within contact distance  $2r_c$ , where  $r_c = 0.15$  is taken as the contact radius. The edge units they belong to must not be connected and should be well aligned. The rate constants for fusion depend on the bending angles that would arise at the newly formed junctions, as given in Eq. (4). The probability of a pair fusing during time step  $\Delta t$  is computed according to:

$$p_{ui} = 1 - \exp\left(-k_{ui}^{\text{eff}} \Delta t\right).$$

Similarly, during each time step, each degree-2 and degree-3 node have a probability of fission given by

$$p_{f2} = 1 - \exp(-k_f \Delta t), \quad p_{f3} = 1 - \exp(-3/2k_f \Delta t),$$

respectively. Following fission, the newly formed nodes are placed just outside of steric overlap  $(d_{i,j} = 2r_s)$ . Details of node placement during fusion and fission, as well as angle calculations defining the fusion rate constants, are given in the Supplemental Material [49]. At most one fission or fusion event can occur per each pair of nodes within a single time step.

Simulations were initialized with a fully fragmented network (in keeping with the mitochondrial fragmentation that occurs prior to cell division [97,98]) and were run for at least  $2 \times 10^6$  time steps. The last 30% of the time-course was used to compute steady-state metrics, and the results were averaged over at least three independent trials for each simulation. The robustness of the resulting structures to different initial conditions is demonstrated in Supplemental Material Fig. S7 [49].

# B. Cell culture, imaging, mitochondrial network extraction, and fusion quantification for COS-7 cells

#### 1. Network extraction

COS-7 cells were grown in Dulbecco's modified Eagle's medium (DMEM) supplemented with 10% fetal bovine serum and maintained in culture for a maximum of 20 passages. 72 h before imaging, cells were seeded in a six-well plate at 70 000 cells per well. 48 h before imaging, cells were transfected with mito-mScarlet (pMTS\_mScarlet\_N1), a gift from Dorus Gadella (Addgene plasmid #85057) with Lipofectamine 2000 (Invitrogen) [99] in Opti-MEM medium (Invitrogen) following the manufacturer's instructions. Cells were grown and handled as in Ref. [21].

To facilitate imaging of whole mitochondrial networks, cells were seeded on fibronectin micropatterned coverslips (made as described here [100]) the evening before imaging (approximately 16 h).

Mitochondrial networks were acquired on a Nikon Eclipse Ti2-E inverted microscope spinning disk CSU-W1 equipped with an sCMOS camera (Photometrics Prime 95B) and a  $100 \times 1.49$  NA oil immersion objective (SR HP Apo TIRF  $100 \times /1.49$ , Nikon). Images were acquired in 100-nm z steps at 37 °C and 5% CO<sub>2</sub> in phenol-red-free DMEM. Before further processing, the RAW images were cropped and deconvolved with Huygens Core, offered by the EPFL imag-

ing core facility (BIOP), using a theoretical point spread function.

To receive the graph output the deconvolved *z*-stacks were processed by Mitograph [101] running via the Windows subsystem for Linux (WSL2). Tiff stacks were processed with the following command:./MitoGraph -xy 0.11 -z 0.1 -labels\_off -path < file-path >.

#### 2. Fusion quantification

The following plasmids and reagents were used to label mitochondria in COS-7 cells. Mito-GFP (Cox-8 presequence) was a gift from H. Shroff (NIH, Bethesda, USA), FASTKD2-EGPF was a gift from J.-C. Martinou, mtAT1.03 was a gift from Hiromi Imamura (Kyoto University, Japan), mito-TagRFP was generated in the laboratory from mito-GFP, TOM20-mCherry, TOM20-EGFP, and TMRE (Sigma, 87917, 500 nM for 10 min and rinsed by PBS). In addition to fluorescent labeling, mitochondria were also imaged by phasecontrast. Transfections were performed using Lipofectamine 2000 (Invitrogen, 11668027) following the manufacturers protocol. Live-cell time series were acquired on a custom-built instant structured illumination microscope [102], a 3D NSIM Nikon inverted fluorescence microscope (Eclipse Ti), a Leica TCS SP8 inverted confocal microscope and a Zeiss Axio Observer 7 inverted widefield microscope. Fusions were manually detected and classified by fusion type using Fiji [103]. Mitochondrial fusions were defined as events where two individual mitochondria came together and formed a single unit that remained clearly connected for several frames following the fusion event. For visualization, noise was removed from representative images with a 1-pixel mean filter. Some data used for this fusion quantification was reused from Rey et al. [104] and Kleele *et al.* [21].

### C. Quantifying experimental network structures

The three data sets referenced in this work are: (1) A set of 93 consecutive network structures for a single hiPSC cell (3.253 seconds per frame), published in Ref. [7] and available on the MitoTNT github page. (2) A set of 2878 *S. cerevisiae* budding yeast networks, of which 2794 are used for the full analysis (keeping only networks with  $\rho_1$ ,  $\rho_2$ ,  $\rho_3 > 0$ ). These structures are accessible via the Mendeley Data webpage associated with Ref. [11]. (3) A set of 37 structures from COS-7 cells, obtained as described above. Mammalian network structures and custom MATLAB code for their handling and analysis are provided on GitHub [93].

In order to compare our simulated networks to experimental data, we compute an approximate mitochondrial volume density for both mammalian-cell data sets. The total mitochondrial length is found as the sum of the edge lengths in each network. For the hiPSC and COS-7 mammalian networks, we found mean mitochondrial lengths ( $\pm$  standard deviation):  $L=360\pm10~\mu m$  and  $L=700\pm200~\mu m$ , respectively. As the precise cytoplasmic volumes accessible to the mitochondria were not directly available from the experimental data, we used a convex hull approach (MATLAB's "boundary" function [92]) to approximate the cytoplasmic volumes. This gave mean volumes:  $1500\pm100~\mu m^3$  and  $3000\pm1000~\mu m^3$ , respectively.

The corresponding length density of mitochondria is then  $\ell_0\hat{\rho}\approx 0.24~\mu\text{m}^{-2}$ . We use a similar density in our simulations, where  $\ell_0\hat{\rho}\approx \ell_0\times 250$  units  $/(\frac{4}{3}\pi R_{\text{cell}}^3)\approx 0.24~\mu\text{m}^{-2}$ . For yeast cells, the distribution of mitochondrial lengths was double peaked, and our density estimates were taken from the subset of cells corresponding to the peak with larger mitochondrial length. For these cells, the average mitochondrial length was  $L=60\pm 20~\mu\text{m}$  (mean  $\pm$  standard deviation) As yeast mitochondria reside predominantly on the inner surface of the cell membrane, we used cell surface area (provided in the dataset) to set the size of our simulated cells. The average surface area for the analyzed cells was  $70\pm 20~\mu\text{m}^2$ , corresponding to a simulation sphere of radius  $R_{\text{cell}}\approx 2.3~\mu\text{m}$ .

To calculate the mean segment length  $\langle L_{\rm seg} \rangle$  and largest cluster size fraction  $\langle L_G/L \rangle$  for the imaged datasets, we use the same procedure as outlined for simulated networks. Estimating association constants  $C_i$  for experimental networks requires first computing the equivalent number of nodes in the imaged network structure. The mitograph structures are analyzed to count the number of degree-1 nodes  $(X_1)$  and the number of higher-degree junctions  $(X_k$  for  $k \geq 3)$ , as well as the total length L of the mitochondria. We then compute the effective number of mitochondrial units  $(N^{\rm eff})$  and effective degree-2, degree-3 nodes  $(X_{2.3}^{\rm eff})$  as follows:

$$N^{\text{eff}} = L/\ell_0$$
 $X_1^{\text{eff}} = X_1$ 
 $X_3^{\text{eff}} = \frac{1}{3} \sum_{k=3}^{\infty} kX_k$ 
 $X_2^{\text{eff}} = N^{\text{eff}} - \frac{1}{2} X_1^{\text{eff}} - \frac{3}{2} X_3^{\text{eff}}.$  (11)

This conversion enables us to calculate  $\hat{\rho}C_i$  for each experimental network in a way that accurately reflects the connectivity of the mitochondria.

## D. Estimation of contact volume and mean fusion rate constants for equilibrium association constants $\widetilde{C}_i$

### 1. 3D networks

The extent of fusion into degree-2 and degree-3 junctions can be described by the effective association constants  $C_1$ ,  $C_2$ , defined by the steady-state ratio of global fusion and fission rate constants [Eq. (6)] or equivalently by ratios of nodes of different degrees. The global fusion rate constant in a well-mixed equilibrium system should be determined by the microscopic angle-dependent fusion rate constants  $k_{ui}^{\rm eff}$ , and the volume of the contact zone within which fusion is possible.

The contact volume  $v_{\mathrm{cont},i}$  is the volume surrounding a degree-1 (or -2) node in which a degree-1 node could be placed such that a valid tip-tip (or tip-side) fusion could occur. This volume is limited by a sphere of radius  $2r_c$ , which defines the contact distance between two nodes. The steric exclusion between two mitochondrial segments reduces the actual configurational volume within which two nodes can fuse. For tip-tip fusion, this reduction involves subtracting the volume of a spherocylinder tip of radius  $2r_s$  (where  $r_s = 0.1 \, \mu \mathrm{m}$ ). For

tip-side fusion we consider the approximation of a perfectly straight existing degree-2 junction to subtract a cylindrical volume of radius  $2r_s$  (see Supplemental Material Fig. S3 for diagram [49]). The contact volumes for each type of fusion are then given by:

$$v_{\text{cont},1} = \frac{2}{3}\pi\{[(2r_c)^2 - (2r_s)^2]^{3/2} + (2r_c)^3 - (2r_s)^3\}$$

$$v_{\text{cont},2} = \frac{4}{3}\pi[(2r_c)^2 - (2r_s)^2]^{3/2}.$$
(12)

The quantity,  $\langle k_{ui}^{\rm eff} \rangle$ , represents the mean fusion rate for a pair of nodes, given that the pair is within contact range. This rate depends on the orientations of the edges attached to the prospective fusing nodes. For tip-tip fusion, we consider an existing edge aligned along the z axis with a second edge fusing in with orientation  $(\theta_2, \phi)$ . The nearest node of the incoming edge is taken to be at a location  $(2r_s + \delta(\theta_1))(\sin\theta_1, 0, \cos\theta_1)$  where  $\delta(\theta_1)$  is set to the average value for a uniform radial distribution within the contact zone at angle  $\theta_1$ . The fusion rate constant  $k_{u,1}^{\rm eff}$  [Eq. (4a)] is averaged over all incoming edge orientations, assumed uniformly distributed, to give:

$$\langle k_{u1}^{\text{eff}} \rangle = \frac{k_{u1}}{4\pi (1 - \rho_1^*)} \int_{\rho_1^*}^1 d\rho_1 \int_{-1}^1 d\rho_2 \int_{-1}^1 d\phi \, e^{-\alpha_1 (1 - \cos \theta^{(1)})}, \tag{13}$$

where  $\rho_i = \cos \theta_i$ ,  $\rho_1^* = -\sqrt{1 - r_s^2/r_c^2}$  is a cutoff for steric exclusion,  $\theta^{(1)}$  is the angle between the fusing edges (dependent on  $\theta_1$ ,  $\theta_2$ ,  $\phi$ ) and  $\alpha_1$  is the angular sensitivity parameter. The resulting equilibrium association constant  $\widetilde{C}_1 = \langle k_{u1}^{\text{eff}} \rangle v_{\text{cont}}/k_f$  defines the linear estimate plotted in Fig. 3(a). The correction factors  $p_{\text{esc}}$ ,  $p_{\text{esc}}^*$  accounting for nonequilibrium effects are described in the Supplemental Material [49].

For tip-side fusion, we employ an analogous strategy to estimate the effective fusion rate constant. The degree-2 node is placed at the origin and the incoming degree-1 node is taken to be at distance  $2r_s + \delta$  (along the negative x axis), where  $\delta$  is set to the average value for a uniform distribution within the contact volume. The first edge is taken to lie along the z axis, and the second edge to be connected at angle  $\theta^{(1)}$ , in the xz plane. The incoming third edge is taken to have polar angle  $\theta_2$  and azimuthal angle  $\phi$  relative to the plane formed by the first two edges. To avoid steric overlap, the azimuthal angle is limited to be between  $(\phi^*, 2\pi - \phi^*)$  where  $\sin \phi^* = 2r_s/(2r_s + \delta)$ . Junction configurations are not equally likely and must be weighed by the appropriate Boltzmann factor depending on the bending angle  $\theta^{(1)}$  and bending stiffness  $B_1$ . We therefore compute:

$$\langle k_{u2}^{\text{eff}} \rangle = k_{u2} \frac{1}{Z} \int_{\phi^*}^{2\pi - \phi^*} d\phi \int_{-1}^{1} d(\cos \theta^{(1)}) \int_{-1}^{1} d(\cos \theta^{(2)}) \times e^{\frac{B_1}{k_b T \ell_0} \cos \theta^{(1)} - \alpha_2 [2 - \cos(\theta^{(2)} - \frac{\pi}{3}) - \cos(\theta^{(3)} - \frac{\pi}{3})]}$$

$$Z = 4\pi \int_{-1}^{1} d(\cos \theta^{(1)}) e^{\frac{B_1}{k_b T \ell_0} \cos \theta^{(1)}},$$
(14)

where  $\theta^{(1)}$  is the angle between the two connected edges, and  $\theta^{(2)}$ ,  $\theta^{(3)}$  are the angles of the incoming edge with each of the two connected ones. The resulting equilibrium association constant  $\widetilde{C}_2 = \langle k_{u2}^{\rm eff} \rangle v_{\rm cont}/k_f$  defines the linear estimate plotted in Fig. 3(b).

### 2. Surface-bound networks

For surface-bound networks representing yeast mitochondria, the contact volume becomes an area, and the mean fusion rate constant is averaged over two-dimensional configurations. For tip-tip fusion, the contact area corresponds to a circle of radius  $2r_c$  minus an excluded region equal to a rectangle of width  $4r_s$  and a half-circle of radius  $2r_s$  For tip-side fusion, we again take the limit of a perfectly straight existing degree-2 junction and subtract a rectangle of width  $4r_s$  from a circle of radius  $2r_c$ . The contact areas are then given by the following expressions:

$$a_{\text{cont},1} = 4r_c^2 [\pi/2 - \sin^{-1}(r_s/r_c)] - 4r_s^2 \sqrt{(r_c/r_s)^2 - 1}$$

$$+ 2\pi (r_c^2 - r_s^2)$$

$$a_{\text{cont},2} = 2 \{ 4r_c^2 [\pi/2 - \sin^{-1}(r_s/r_c)] - 4r_s^2 \sqrt{(r_c/r_s)^2 - 1} \}.$$
(15)

Due to the higher segment density in the surface-bound case, we explicitly subtract from the total available area the space that is sterically excluded by existing nodes. Specifically, we compute  $\hat{\rho}\widetilde{C}_i = \langle k_{ui}^{\rm eff} \rangle_{\frac{A_{\rm cont},i}{A_{\rm tot}-A_{\rm excl}}}^{\frac{A_{\rm cont},i}{A_{\rm tot}}} / k_f$  where  $A_{\rm excl} = \frac{2}{\pi} (\ell_0 + 2r_s)^2 N_{\rm edge}$  is the approximate excluded area between two rectangles (see Ref. [105], Fig. 14.17) and  $A_{\rm tot} = 4\pi R_{\rm cell}^2$ . In the 3D case, the corresponding correction was found negligible and was ommitted for simplicity.

We also exclude the sterically inaccessible orientational states when integrating over possible incoming node positions and edge orientations to find the average fusion rate constant. For tip-tip fusion, we take the node separation to be  $2r_s + \delta$  as in the 3D calculation above. The first edge lies along the negative x axis with one node at the origin. Equal weights are assigned to all positions  $\vec{r} = (2r_s + \delta)(\cos \phi, \sin \phi)$  and orientations,  $\theta$ :

$$\langle k_{u1}^{\text{eff}} \rangle = k_{u1} \left( \frac{1}{2\pi} \right)^{2} \int_{-\pi + \phi^{*}}^{\pi - \phi^{*}} d\phi \int_{\theta_{1}(\phi, \phi^{*})}^{\theta_{2}(\phi, \phi^{*})} d\theta e^{-\alpha_{1}(1 - \cos \theta)}$$

$$\theta_{1}(\phi, \phi^{*}) = \begin{cases} -\pi, & \text{if } \phi < -\phi^{*} \\ -(\pi - \phi^{*}) + \phi, & \text{if } \phi > -\phi^{*} \end{cases}$$

$$\theta_{2}(\phi, \phi^{*}) = \begin{cases} \pi - \phi^{*} + \phi, & \text{if } \phi < \phi^{*} \\ \pi, & \text{if } \phi > \phi^{*}, \end{cases}$$
(16)

where  $\sin \phi^* = 2r_s/(2r_s + \delta)$  as defined above and integration limits are chosen so as to eliminate sterically forbidden node positions and edge orientations. This result corresponds to the linear prediction in Fig. 4(c).

For tip-side fusion, the effective average fusion rate constant within the contact volume is estimated as follows. We place the incoming degree-1 node at a distance  $2r_s + \delta$  along the positive y axis, with the degree-2 junction at the origin. The first edge lies along the negative x axis, with the second edge connected at angle  $\theta^{(1)}$  The angles  $\theta^{(2)}$ ,  $\theta^{(3)}$  indicate the orientation of the incoming 3rd edge relative to the first and second edges, respectively. Sterically forbidden orientations

are approximately eliminated via the integration limits:

$$\langle k_{u2}^{\text{eff}} \rangle = k_{u2} \frac{1}{Z} \left( \int_{-\pi}^{\pi/2 - \phi^*} d\theta^{(1)} \int_{\max(\theta^{(1)}, -\pi/2 + \phi^*)}^{\pi} d\theta^{(2)} + \int_{\pi/2 + \phi^*}^{\pi} d\theta^{(1)} \int_{-\pi/2 + \phi^*}^{\theta^{(1)}} d\theta^{(2)} \right) \times e^{\frac{B_1}{k_b T \ell_0} (1 - \cos \theta^{(1)}) - \alpha_2 [2 - \cos(\theta^{(2)} - \pi/3) - \cos(\theta^{(3)} - \pi/3)]}$$

$$Z = (2\pi) \int_{0}^{2\pi} d\theta^{(1)} e^{-\frac{B_1}{\ell_0} (1 - \cos \theta^{(1)})/k_b T}. \tag{17}$$

This result gives the linear prediction shown in Fig. 4(d).

## E. Solution to the simplified kinetic model for escape

Here we present the solution to the model diagramed in Fig. 3(b) (inset), which describes the possible states of a single pair of nodes capable of undergoing fusion and fission. The steady-state kinetic equations for this system are

$$\frac{df}{dt} = -k_a f + k_e n + k_e^* n^* = 0$$

$$\frac{dn}{dt} = -(k_u + k_e) n + k_a f = 0$$

$$\frac{dn^*}{dt} = -(k_u + k_e^*) n^* + k_f j = 0$$

$$\frac{dj}{dt} = -k_f j + k_u (n + n^*) = 0$$

$$f + n + n^* + j = 1,$$
(18)

where the variables j, n,  $n^*$ , f are the probabilites of finding the pair in the corresponding state. The association constants  $C_1$ ,  $C_2$  (scaled by the volume of the domain) measure the ratio of fused to unfused node pairs, and may therefore be written generically in terms of the state probabilites:

$$C/V = \frac{j}{1-j} = \frac{k_u}{k_f} \frac{1/p_{\rm esc}^*}{(k_u + k_e)/k_a + 1/p_{\rm esc}^*},$$
 (19)

where  $p_{\rm esc}^* = k_e^*/(k_u + k_e^*)$ . A simpler equilibrium system obeying detailed balance would be one where fission returns the node pair to the same state it was in immediately before fusion, so that  $n^* \to n$  and  $k_e^* \to k_e$ . In this equilibrium case, the fraction of disjoint pairs that are close enough to enable fusion must equal the volume fraction of the contact zone:  $n_{\rm eq}/(f_{\rm eq} + n_{\rm eq}) = k_a/(k_a + k_e) = v_{\rm cont}/V$ . The association constants may then be expressed as:

$$C/V = \frac{k_u}{k_f} \frac{v_{\text{cont}}}{V} \frac{1 + k_a/k_e}{p_{\text{esc}}^*(k_u + k_e)/k_e + k_a/k_e}$$
$$= \frac{k_u}{k_f} \frac{v_{\text{cont}}}{V} \frac{1 + k_a/k_e}{p_{\text{esc}}^*/p_{\text{esc}} + k_a/k_e}, \tag{20}$$

where  $p_{\rm esc} = k_e/(k_u + k_e)$  is the escape probability for the equilibrated reaction which retains no memory of prior fission.

In the relevant limit of the domain size much larger than the size of an individual mitochondrion, we have  $v_{\rm cont} \ll V$  and hence  $k_a \ll k_e$ . Consequently, we can estimate the overall

association constants as:

$$\widehat{C} \approx \frac{k_u v_{\text{cont}}}{k_f} \frac{p_{\text{esc}}}{p_{\text{esc}}^*}.$$
 (21)

We note that escape is less likely immediately after a fission event, because the nodes are more closely positioned (separation  $2r_s$ ) than they were on fusion and the orientation of the segments tends to be more favorable for refusion. Because the correction factor  $p_{\rm esc}/p_{\rm esc}^* > 1$  itself increases with rising fusion rate constant, it allows for a super-linear dependence of the associaton constant on the microscopic fusion rate constant  $k_u$ .

In this simplified model, the fusion rate constant  $k_u$  incorporates rates  $k_{ui}^{\text{eff}}$  averaged over possible orientations of newly

approaching segments [Eqs. (13), (14), (16), and (17)]. The escape probabilities must be computed by considering the initial separation of the two nodes within contact range, and their alignment for subsequent refusion. Approximations for these quantities are derived from a reaction-diffusion model in spherical coordinates, as detailed in the Supplemental Material [49].

#### ACKNOWLEDGMENTS

We thank Zubenelgenubi Scott, Padmini Rangamani, and members of the Rangamani group for helpful discussions. This work was supported by NSF (Grants No. 2310229 and No. 1848057), and an award from the Chan Zuckerberg Initiative (Grant No. 2023-329599).

- [1] A. S. Monzel, J. A. Enríquez, and M. Picard, Multifaceted mitochondria: Moving mitochondrial science beyond function and dysfunction, Nature Metab. 5, 546 (2023).
- [2] G. Twig, A. Elorza, A. J. Molina, H. Mohamed, J. D. Wikstrom, G. Walzer, L. Stiles, S. E. Haigh, S. Katz, G. Las *et al.*, Fission and selective fusion govern mitochondrial segregation and elimination by autophagy, EMBO J. 27, 433 (2008).
- [3] B. Westermann, Mitochondrial fusion and fission in cell life and death, Nat. Rev. Mol. Cell Biol. 11, 872 (2010).
- [4] L. C. Gomes, G. D. Benedetto, and L. Scorrano, During autophagy mitochondria elongate, are spared from degradation and sustain cell viability, Nature Cell Biol. 13, 589 (2011).
- [5] R. J. Youle and A. M. Van Der Bliek, Mitochondrial fission, fusion, and stress, Science 337, 1062 (2012).
- [6] B. Spurlock, P. Gupta, M. K. Basu, A. Mukherjee, A. B. Hjelmeland, V. Darley-Usmar, D. Parker, M. E. Foxall, and K. Mitra, New quantitative approach reveals heterogeneity in mitochondrial structure–function relations in tumor-initiating cells, J. Cell Sci. 132, jcs230755 (2019).
- [7] Z. Wang, P. Natekar, C. Tea, S. Tamir, H. Hakozaki, and J. Schöneberg, MitoTNT: Mitochondrial temporal network tracking for 4D live-cell fluorescence microscopy data, PLoS Comput. Biol. 19, e1011060 (2023).
- [8] A. R. Fenton, T. A. Jongens, and E. L. Holzbaur, Mitochondrial dynamics: Shaping and remodeling an organelle network, Curr. Opin. Cell Biol. 68, 28 (2021).
- [9] P. K. Patel, O. Shirihai, and K. C. Huang, Optimal dynamics for quality control in spatially distributed mitochondrial networks, PLoS Comput. Biol. 9, e1003108 (2013).
- [10] M. Guo, A. J. Ehrlicher, M. H. Jensen, M. Renz, J. R. Moore, R. D. Goldman, J. Lippincott-Schwartz, F. C. Mackintosh, and D. A. Weitz, Probing the stochastic, motor-driven properties of the cytoplasm using force spectrum microscopy, Cell 158, 822 (2014).
- [11] M. P. Viana, A. I. Brown, I. A. Mueller, C. Goul, E. F. Koslover, and S. M. Rafelski, Mitochondrial fission and fusion dynamics generate efficient, robust, and evenly distributed network topologies in budding yeast cells, Cell Syst. 10, 287 (2020).

- [12] H. Hoitzing, I. G. Johnston, and N. S. Jones, What is the function of mitochondrial networks? a theoretical assessment of hypotheses and proposal for future research, BioEssays 37, 687 (2015).
- [13] S. Mai, M. Klinkenberg, G. Auburger, J. Bereiter-Hahn, and M. Jendrach, Decreased expression of Drp1 and Fis1 mediates mitochondrial elongation in senescent cells and enhances resistance to oxidative stress through PINK1, J. Cell Sci. 123, 917 (2010).
- [14] M. Liesa and O. S. Shirihai, Mitochondrial dynamics in the regulation of nutrient utilization and energy expenditure, Cell Metab. 17, 491 (2013).
- [15] G. Szabadkai, A. M. Simoni, M. Chami, M. R. Wieckowski, R. J. Youle, and R. Rizzuto, Drp-1-dependent division of the mitochondrial network blocks intraorganellar Ca<sup>2+</sup> waves and protects against Ca<sup>2+</sup>-mediated apoptosis, Mol. Cell 16, 59 (2004).
- [16] F. Fischer, A. Hamann, and H. D. Osiewacz, Mitochondrial quality control: An integrated network of pathways, Trends Biochem. Sci. 37, 284 (2012).
- [17] A. Scally and R. Durbin, Revising the human mutation rate: implications for understanding human evolution, Nat. Rev. Genet. 13, 745 (2012).
- [18] V. Wilkens, W. Kohl, and K. Busch, Restricted diffusion of oxphos complexes in dynamic mitochondria delays their exchange between cristae and engenders a transitory mosaic distribution, J. Cell Sci. 126, 103 (2013).
- [19] H. Chen, M. Vermulst, Y. E. Wang, A. Chomyn, T. A. Prolla, J. M. McCaffery, and D. C. Chan, Mitochondrial fusion is required for mtDNA stability in skeletal muscle and tolerance of mtDNA mutations, Cell 141, 280 (2010).
- [20] A. Kowald and T. B. Kirkwood, Evolution of the mitochondrial fusion–fission cycle and its role in aging, Proc. Natl. Acad. Sci. USA 108, 10237 (2011).
- [21] T. Kleele, T. Rey, J. Winter, S. Zaganelli, D. Mahecic, H. Perreten Lambert, F. P. Ruberto, M. Nemir, T. Wai, T. Pedrazzini *et al.*, Distinct fission signatures predict mitochondrial degradation or biogenesis, Nature (Lond.) **593**, 435 (2021).

- [22] I. Kim, S. Rodriguez-Enriquez, and J. J. Lemasters, Selective degradation of mitochondria by mitophagy, Arch. Biochem. Biophys. **462**, 245 (2007).
- [23] A. Bratic and N.-G. Larsson, The role of mitochondria in aging, J. Clin. Invest. 123, 951 (2013).
- [24] W. Wang, F. Zhao, X. Ma, G. Perry, and X. Zhu, Mitochon-dria dysfunction in the pathogenesis of Alzheimer's disease: Recent advances, Mol. Neurodegener. 15, 30 (2020).
- [25] J.-S. Park, R. L. Davis, and C. M. Sue, Mitochondrial dysfunction in Parkinson's disease: new mechanistic insights and therapeutic perspectives, Curr. Neurol. Neurosci. 18, 21 (2018).
- [26] M. Filosto, M. Scarpelli, M. S. Cotelli, V. Vielmi, A. Todeschini, V. Gregorelli, P. Tonin, G. Tomelleri, and A. Padovani, The role of mitochondria in neurodegenerative diseases, J. Neurol. 258, 1763 (2011).
- [27] F. Burté, V. Carelli, P. F. Chinnery, and P. Yu-Wai-Man, Disturbed mitochondrial dynamics and neurodegenerative disorders, Nat. Rev. Neurol. 11, 11 (2015).
- [28] H. Chen and D. C. Chan, Mitochondrial dynamics-fusion, fission, movement, and mitophagy-in neurodegenerative diseases, Hum. Mol. Genet. 18, R169 (2009).
- [29] N. Zamponi, E. Zamponi, S. A. Cannas, O. V. Billoni, P. R. Helguera, and D. R. Chialvo, Mitochondrial network complexity emerges from fission/fusion dynamics, Sci. Rep. 8, 363 (2018).
- [30] D. Otsuga, B. R. Keegan, E. Brisch, J. W. Thatcher, G. J. Hermann, W. Bleazard, and J. M. Shaw, The dynamin-related GTPase, Dnm1p, controls mitochondrial morphology in yeast, J. Cell Biol. 143, 333 (1998).
- [31] S. Li, S. Xu, B. A. Roelofs, L. Boyman, W. J. Lederer, H. Sesaki, and M. Karbowski, Transient assembly of f-actin on the outer mitochondrial membrane contributes to mitochondrial fission, J. Cell Biol. 208, 109 (2015).
- [32] T. Tsuboi, M. P. Viana, F. Xu, J. Yu, R. Chanchani, X. G. Arceo, E. Tutucci, J. Choi, Y. S. Chen, R. H. Singer *et al.*, Mitochondrial volume fraction and translation duration impact mitochondrial mRNA localization and protein synthesis, Elife 9, e57814 (2020).
- [33] A. S. Rambold, B. Kostelecky, N. Elia, and J. Lippincott-Schwartz, Tubular network formation protects mitochondria from autophagosomal degradation during nutrient starvation, Proc. Natl. Acad. Sci. USA 108, 10190 (2011).
- [34] D. A. Patten, J. Wong, M. Khacho, V. Soubannier, R. J. Mailloux, K. Pilon-Larose, J. G. MacLaurin, D. S. Park, H. M. McBride, L. Trinkle-Mulcahy *et al.*, Opa1-dependent cristae modulation is essential for cellular adaptation to metabolic demand, EMBO J. 33, 2676 (2014).
- [35] Y. Zhao, M. Zhang, W. Zhang, Y. Zhou, L. Chen, Q. Liu, P. Wang, R. Chen, X. Duan, F. Chen *et al.*, Isotropic superresolution light-sheet microscopy of dynamic intracellular structures at subsecond timescales, Nature Methods 19, 359 (2022).
- [36] V. M. Sukhorukov, D. Dikov, A. S. Reichert, and M. Meyer-Hermann, Emergence of the mitochondrial reticulum from fission and fusion dynamics, PLoS Comput. Biol. 8, e1002745 (2012).
- [37] P. K. Mouli, G. Twig, and O. S. Shirihai, Frequency and selectivity of mitochondrial fusion are key to its quality maintenance function, Biophys. J. **96**, 3509 (2009).

- [38] V. M. Sukhorukov and M. Meyer-Hermann, Structural heterogeneity of mitochondria induced by the microtubule cytoskeleton, Sci. Rep. 5, 13924 (2015).
- [39] R. C. Glastad and I. G. Johnston, Mitochondrial network structure controls cell-to-cell mtDNA variability generated by cell divisions, PLoS Comput. Biol. 19, e1010953 (2023).
- [40] S. Babu, M. Rottereau, T. Nicolai, J. C. Gimel, and D. Durand, Flocculation and percolation in reversible cluster-cluster aggregation, Eur. Phys. J. E 19, 203 (2006).
- [41] E. Dickinson, Structure and rheology of simulated gels formed from aggregated colloidal particles, J. Colloid Interface Sci. **225**, 2 (2000).
- [42] S. R. Broadbent and J. M. Hammersley, Percolation processes: I. crystals and mazes, in *Mathematical Proceedings of* the Cambridge Philosophical Society (Cambridge University Press, Cambridge, UK, 1957), Vol. 53, pp. 629–641.
- [43] D. Stauffer and A. Aharony, *Introduction to Percolation Theory* (CRC Press, Boca Raton, FL, 2018).
- [44] N. Seaton and E. D. Glandt, Aggregation and percolation in a system of adhesive spheres, J. Chem. Phys. 86, 4668 (1987).
- [45] E. J. Garboczi, K. A. Snyder, J. F. Douglas, and M. F. Thorpe, Geometrical percolation threshold of overlapping ellipsoids, Phys. Rev. E 52, 819 (1995).
- [46] I. Balberg, N. Binenbaum, and N. Wagner, Percolation thresholds in the three-dimensional sticks system, Phys. Rev. Lett. 52, 1465 (1984).
- [47] Y.-B. Huang and P. Somasundaran, Effects of random-walk size on the structure of diffusion-limited aggregates, Phys. Rev. A 36, 4518 (1987).
- [48] J. Nicolás-Carlock, J. Carrillo-Estrada, and V. Dossetti, Fractality à la carte: A general particle aggregation model, Sci. Rep. 6, 19505 (2016).
- [49] See Supplemental Material at http://link.aps.org/supplemental/ 10.1103/PRXLife.2.043002 for further details regarding simulation methods and parameter selection, which includes Refs. [50–54].
- [50] T. S. Fung, R. Chakrabarti, and H. N. Higgs, The multiple links between actin and mitochondria, Nat. Rev. Mol. Cell Biol. 24, 651 (2023).
- [51] S.-H. Lee, K. Palmo, and S. Krimm, New out-of-plane angle and bond angle internal coordinates and related potential energy functions for molecular mechanics and dynamics simulations, J. Comput. Chem. 20, 1067 (1999).
- [52] A. B. Fernández Casafuz, M. C. De Rossi, and L. Bruno, Mitochondrial cellular organization and shape fluctuations are differentially modulated by cytoskeletal networks, Sci. Rep. 13, 4065 (2023).
- [53] D. W. Hahn and M. N. Özisik, *Heat Conduction* (John Wiley & Sons, New York, 2012).
- [54] S. Redner, A Guide to First-Passage Processes (Cambridge University Press, Cambridge, UK, 2001).
- [55] S. M. Rafelski, M. P. Viana, Y. Zhang, Y.-H. M. Chan, K. S. Thorn, P. Yam, J. C. Fung, H. Li, L. d. F. Costa, and W. F. Marshall, Mitochondrial network size scaling in budding yeast, Science 338, 822 (2012).
- [56] A. Kaasik, D. Safiulina, A. Zharkovsky, and V. Veksler, Regulation of mitochondrial matrix volume, Am. J. Physiol. Cell Physiol. 292, C157 (2007).
- [57] S. Jakobs and C. A. Wurm, Super-resolution microscopy of mitochondria, Curr. Opin. Chem. Biol. 20, 9 (2014).

- [58] E. F. Koslover and A. J. Spakowitz, Discretizing elastic chains for coarse-grained polymer models, Soft Matter 9, 7016 (2013).
- [59] T. Kim, W. Hwang, H. Lee, and R. D. Kamm, Computational analysis of viscoelastic properties of crosslinked actin networks, PLoS Comput. Biol. 5, e1000439 (2009).
- [60] G. Twig, X. Liu, M. Liesa, J. D. Wikstrom, A. J. Molina, G. Las, G. Yaniv, G. Hajnóczky, and O. S. Shirihai, Biophysical properties of mitochondrial fusion events in pancreatic β-cells and cardiac cells unravel potential control mechanisms of its selectivity, Am. J. Physiol. Cell Physiol. 299, C477 (2010).
- [61] K. Mehta, L. A. Chacko, M. K. Chug, S. Jhunjhunwala, and V. Ananthanarayanan, Association of mitochondria with microtubules inhibits mitochondrial fission by precluding assembly of the fission protein Dnm1, J. Biol. Chem. 294, 3385 (2019).
- [62] M. T. Figge, A. S. Reichert, M. Meyer-Hermann, and H. D. Osiewacz, Deceleration of fusion–fission cycles improves mitochondrial quality control during aging, PLoS Comput. Biol. 8, e1002576 (2012).
- [63] K. Kornick, B. Bogner, L. Sutter, and M. Das, Population dynamics of mitochondria in cells: A minimal mathematical model, Front. Phys. 7, 146 (2019).
- [64] B. Corci, O. Hooiveld, A. M. Dolga, and C. Åberg, Extending the analogy between intracellular motion in mammalian cells and glassy dynamics, Soft Matter 19, 2529 (2023).
- [65] D. H. Jang, S. C. Seeger, M. E. Grady, F. S. Shofer, and D. M. Eckmann, Mitochondrial dynamics and respiration within cells with increased open pore cytoskeletal meshes, Biol. Open 6, 1831 (2017).
- [66] E. Zaccarelli, S. V. Buldyrev, E. La Nave, A. J. Moreno, I. Saika-Voivod, F. Sciortino, and P. Tartaglia, Model for reversible colloidal gelation, Phys. Rev. Lett. 94, 218301 (2005).
- [67] M. A. Aon, S. Cortassa, and B. O'Rourke, Percolation and criticality in a mitochondrial network, Proc. Natl. Acad. Sci. USA 101, 4447 (2004).
- [68] P. Blatz and A. Tobolsky, Note on the kinetics of systems manifesting simultaneous polymerization-depolymerization phenomena, J. Phys. Chem. 49, 77 (1945).
- [69] J. M. Andrews and C. J. Roberts, A Lumry-Eyring nucleated polymerization model of protein aggregation kinetics: 1. Aggregation with pre-equilibrated unfolding, J. Phys. Chem. B 111, 7897 (2007).
- [70] Z. Budrikis, G. Costantini, C. A. La Porta, and S. Zapperi, Protein accumulation in the endoplasmic reticulum as a nonequilibrium phase transition, Nat. Commun. 5, 3620 (2014).
- [71] L. Onsager, Reciprocal relations in irreversible processes. i., Phys. Rev. **37**, 405 (1931).
- [72] T. L. Hill, Free Energy Transduction and Biochemical Cycle Kinetics (Courier Corporation, North Chelmsford, MA, 2013).
- [73] S. L. Meeusen and J. Nunnari, How mitochondria fuse, Curr. Opin. Cell Biol. 17, 389 (2005).
- [74] B. R. Parry, I. V. Surovtsev, M. T. Cabeen, C. S. O'Hern, E. R. Dufresne, and C. Jacobs-Wagner, The bacterial cytoplasm has glass-like properties and is fluidized by metabolic activity, Cell 156, 183 (2014).
- [75] S. K. Gupta and M. Guo, Equilibrium and out-of-equilibrium mechanics of living mammalian cytoplasm, J. Mech. Phys. Solids 107, 284 (2017).
- [76] C. Lin, M. Schuster, S. C. Guimaraes, P. Ashwin, M. Schrader, J. Metz, C. Hacker, S. J. Gurr, and G. Steinberg, Active

- diffusion and microtubule-based transport oppose myosin forces to position organelles in cells, Nat. Commun. 7, 11814 (2016).
- [77] D. Posey, P. Blaisdell-Pijuan, S. K. Knoll, T. A. Saif, and W. W. Ahmed, Small-scale displacement fluctuations of vesicles in fibroblasts, Sci. Rep. 8, 13294 (2018).
- [78] M. Picard and C. Sandi, The social nature of mitochondria: Implications for human health, Neurosci. Biobehav. Rev. 120, 595 (2021).
- [79] J. M. Chustecki, D. J. Gibbs, G. W. Bassel, and I. G. Johnston, Network analysis of arabidopsis mitochondrial dynamics reveals a resolved tradeoff between physical distribution and social connectivity, Cell Syst. 12, 419 (2021).
- [80] P. Ježek and A. Dlasková, Dynamic of mitochondrial network, cristae, and mitochondrial nucleoids in pancreatic  $\beta$ -cells, Mitochondrion **49**, 245 (2019).
- [81] M. M. Lin, Circuit reduction of heterogeneous nonequilibrium systems, Phys. Rev. Lett. 125, 218101 (2020).
- [82] J. Estrada, F. Wong, A. DePace, and J. Gunawardena, Information integration and energy expenditure in gene regulation, Cell 166, 234 (2016).
- [83] E. Arunachalam and M. M. Lin, A thermodynamic limit on molecular computation, arXiv:2311.15378.
- [84] R. G. Abrisch, S. C. Gumbin, B. T. Wisniewski, L. L. Lackner, and G. K. Voeltz, Fission and fusion machineries converge at ER contact sites to regulate mitochondrial morphology, J. Cell Biol. 219, e201911122 (2020).
- [85] M. Karbowski, D. Arnoult, H. Chen, D. C. Chan, C. L. Smith, and R. J. Youle, Quantitation of mitochondrial dynamics by photolabeling of individual organelles shows that mitochondrial fusion is blocked during the Bax activation phase of apoptosis, J. Cell Biol. 164, 493 (2004).
- [86] X. Liu, D. Weaver, O. Shirihai, and G. Hajnóczky, Mitochondrial 'kiss-and-run': interplay between mitochondrial motility and fusion–fission dynamics, EMBO J. 28, 3074 (2009).
- [87] S. B. Berman, Y.-b. Chen, B. Qi, J. M. McCaffery, E. B. Rucker III, S. Goebbels, K.-A. Nave, B. A. Arnold, E. A. Jonas, F. J. Pineda *et al.*, Bcl-xl increases mitochondrial fission, fusion, and biomass in neurons, J. Cell Biol. 184, 707 (2009).
- [88] T. Klecker and B. Westermann, Asymmetric inheritance of mitochondria in yeast, Biol. Chem. 401, 779 (2020).
- [89] T. Misgeld and T. L. Schwarz, Mitostasis in neurons: Maintaining mitochondria in an extended cellular architecture, Neuron **96**, 651 (2017).
- [90] X. G. Arceo, E. F. Koslover, B. M. Zid, and A. I. Brown, Mitochondrial mRNA localization is governed by translation kinetics and spatial transport, PLoS Comput. Biol. 18, e1010413 (2022).
- [91] W. A. Prinz, A. Toulmay, and T. Balla, The functional universe of membrane contact sites, Nat. Rev. Mol. Cell Biol. **21**, 7 (2020).
- [92] T. M. Inc., Matlab version: 9.13.0 (r2022b) (2022).
- [93] Simulation code and mammalian network structures are provided at https://github.com/lenafabr/mitochondrialNetworks.
- [94] M. Somasi, B. Khomami, N. J. Woo, J. S. Hur, and E. S. Shaqfeh, Brownian dynamics simulations of bead-rod and bead-spring chains: Numerical algorithms and coarse-graining issues, J. Non-Newton. Fluid Mech. 108, 227 (2002).

- [95] J. C. Butcher, Coefficients for the study of Runge-Kutta integration processes, J. Aust. Math. Soc. 3, 185 (1963).
- [96] E. F. Koslover and A. J. Spakowitz, Multiscale dynamics of semiflexible polymers from a universal coarse-graining procedure, Phys. Rev. E **90**, 013304 (2014).
- [97] P. Mishra and D. C. Chan, Mitochondrial dynamics and inheritance during cell division, development and disease, Nat. Rev. Mol. Cell Biol. 15, 634 (2014).
- [98] K. Mitra, C. Wunder, B. Roysam, G. Lin, and J. Lippincott-Schwartz, A hyperfused mitochondrial state achieved at G<sub>1</sub>-S regulates cyclin E buildup and entry into S phase, Proc. Natl. Acad. Sci. USA 106, 11960 (2009).
- [99] D. S. Bindels, L. Haarbosch, L. Van Weeren, M. Postma, K. E. Wiese, M. Mastop, S. Aumonier, G. Gotthard, A. Royant, M. A. Hink *et al.*, mscarlet: A bright monomeric red fluorescent protein for cellular imaging, Nature Methods 14, 53 (2017).
- [100] A. Azioune, N. Carpi, Q. Tseng, M. Théry, and M. Piel, Protein micropatterns: A direct printing protocol using deep UVs, Methods Cell Bio. 97, 133 (2010).

- [101] M. P. Viana, S. Lim, and S. M. Rafelski, Quantifying mitochondrial content in living cells, in *Methods in Cell Biology* (Elsevier, Amsterdam, 2015), Vol. 125, pp. 77–93.
- [102] D. Mahecic, D. Gambarotto, K. M. Douglass, D. Fortun, N. Banterle, K. A. Ibrahim, M. Le Guennec, P. Gönczy, V. Hamel, P. Guichard *et al.*, Homogeneous multifocal excitation for high-throughput super-resolution imaging, Nature Methods 17, 726 (2020).
- [103] J. Schindelin, I. Arganda-Carreras, E. Frise, V. Kaynig, M. Longair, T. Pietzsch, S. Preibisch, C. Rueden, S. Saalfeld, B. Schmid *et al.*, Fiji: an open-source platform for biological-image analysis, Nature Methods 9, 676 (2012).
- [104] T. Rey, S. Zaganelli, E. Cuillery, E. Vartholomaiou, M. Croisier, J.-C. Martinou, and S. Manley, Mitochondrial RNA granules are fluid condensates positioned by membrane dynamics, Nature Cell Biol. 22, 1180 (2020).
- [105] R. Phillips, J. Kondev, J. Theriot, and H. Garcia, *Physical Biology of the Cell* (Garland Science, Milton, Park, UK, 2012).